Nanoscale Advances

ROYAL SOCIETY OF CHEMISTRY

REVIEW

View Article Online
View Journal | View Issue

Cite this: *Nanoscale Adv.*, 2020, **2**, 4323

The highly-efficient light-emitting diodes based on transition metal dichalcogenides: from architecture to performance

Caiyun Wang,[a] Fuchao Yang *[b] and Yihua Gao [a]

Transition metal dichalcogenides (TMDCs) with layered architecture and excellent optoelectronic properties have been a hot spot for light-emitting diodes (LED). However, the light-emitting efficiency of TMDC LEDs is still low due to the large size limit of TMDC flakes and the inefficient device architecture. First and foremost, to develop the highly-efficient and reliable few-layer TMDC LEDs, the modulation of the electronic properties of TMDCs and TMDC heterostructures is necessary. In order to create efficient TMDC LEDs with prominent performance, an in-depth understanding of the working mechanism is needed. Besides conventional structures, the electric (or ionic liquid)-induced p–n junction of TMDCs is a useful configuration for multifunctional LED applications. The significant performances are contrasted in the four aspects of color, polarity, and external quantum efficiency. The color of light ranging from infrared to visible light can be acquired from TMDC LEDs by purposeful and selective architecture construction. To date, the maximum of the external quantum efficiency achieved by TMDC LEDs is 12%. In the demand for performance, the material and configuration of the nano device can be chosen according to this review. Moreover, novel electroluminescence devices involving single-photon emitters and alternative pulsed light emitters can expand their application scope. In this review, we provide an overview of the significant investigations that have provided a wealth of detailed information on TMDC electroluminescence devices at the molecular level.

Received 19th June 2020
Accepted 17th July 2020

DOI: 10.1039/d0na00501k

rsc.li/nanoscale-advances

1. Introduction

Transition metal dichalcogenides (TMDCs) have become a hot spot for two-dimensional material investigations.[1–5] Generally, TMDCs have the chemical formula MX_2, where M = Mo, W, Re, and X = S, Se, Te. The research on TMDCs cover their effective synthesis, excellent optoelectronic properties, and correlative device performance.[6–10] The electronic and optical properties of

[a]*Center for Nanoscale Characterization & Devices (CNCD), School of Physics, Wuhan National Laboratory for Optoelectronics (WNLO), Huazhong University of Science and Technology (HUST), Wuhan 430074, P. R. China*

[b]*Hubei Collaborative Innovation Centre for Advanced Organic Chemical Materials, Ministry of Education Key Laboratory for the Green Preparation and Application of Functional Materials, Hubei University, Wuhan 430062, China. E-mail: yangfuchao163@163.com*

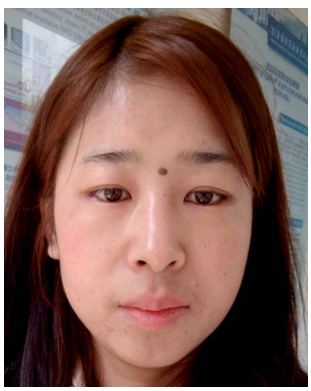

Caiyun Wang joined Prof. Gao's Nanomaterials and Device group at the Huazhong University of Science and Technology (HUST) in 2018 in pursuit of her Ph.D. Her current scientific interests include designing and fabricating 2D materials and 2D material-based light-emitting diodes and studying their corresponding applications.

Dr Fuchao Yang received his Ph.D. from Lanzhou Institute of Chemical Physics (LICP), Chinese Academy of Sciences (CAS) in 2016. Since then, he joined Hubei University. His research interest is focused on the photoelectric behavior of hierarchical surfaces under harsh conditions and fabricating stimuli-responsive surfaces with micro/nanostructures applied for smart functional materials.

TMDCs depend critically on the number of layers, N. For example, the bandgap transforms from the indirect bandgap of TMDCs bulk to the direct bandgap of the monolayer, and for another example, the photoluminescence (PL) quantum yield (QY) of monolayer $MoTe_2$ is approximately three times (forty times) more than that of the bilayer (bulk).[11] Due to their excellent layer shape structure and optoelectronic properties, much research has been conducted on TMDCs-based light-emitting diodes (LED) to date.

The research on TMDCs-based LED is mainly focused on the device structure to acquire an abundant luminous performance. According to different demand and supply, two-dimensional TMDCs can be fabricated with arbitrarily structured material to form heterostructures, such as 2D–2D heterostructures,[12–14] 2D–0D heterostructures,[15–18] 2D–1D heterostructures,[19–21] and 2D–3D heterostructures.[22–24] TMDC heterostructures have been extensively fabricated to achieve special luminescence performance, for instance, high quantum optical properties of single-photon emitters.[24] The heterostructures have also been applied to highly light-sensitive photodetectors.[25,26] In order to be utilized as LEDs, TMDCs have been combined with other materials of different electronic band structure to construct heterostructures. The accessible device architectures include MIS (metal–insulator–semiconductor) junctions, p–n (p-type semiconductor/n-type semiconductor) junctions, and MS (metal–semiconductor) junctions. P–n diodes represent the most common building units for TMDC-based LEDs.[27]

The investigation and improvement in the performances of TMDC-based LEDs are significant for their future applications. The luminescence performances of LEDs include the light-extraction efficiency, external quantum efficiency (EQE), and chroma. Nowadays, less research is conducted on TMDC LEDs and it is not as intensive as that of other light-emitting materials, for example, the ZnO.[28] The EQE of the layered TMDC LED is still low, which restricts its application. In particular, the low QY of 1L-TMDCs is due to the high density of lattice defects. In order to enhance the EQE, the QYs of 1L-TMDCs urgently need to be improved. The QYs of layered-TMDCs have been deeply studied by theoretical calculations and some experimental methods; for example, it was found that oxygen absorbance affects the QY.[29] To build highly-efficient TMDC LEDs, the electrical and optical properties of TMDC heterostructures were studied by density functional theory or first-principles calculation.[30,31] The EL may originate from bound-excitons, defect bound-excitons, hot electrons, and defect-related light.[32] Hong *et al.*[33] studied the energy band gap of monolayer $ReSe_2$ using STM and PL, and the exciton binding energy of $ReSe_2$ was deduced. The defects in TMDC-layered materials have been advantageously explored using STM technology.[33–36]

In this review, we present the electronic properties of TMDCs and the heterostructures studied *via* density functional theory in Section 2. The device configuration and light emission mechanism of TMDC-based LEDs are reviewed in Section 3. The performances of TMDC-based LEDs are analyzed in Section 4. Novel EL devices are reviewed in Section 5. Herein, the prospects of TMDC-based LEDs are also put forward and the challenge will be predicted.

*Prof. Yihua Gao received his Ph.D. at the Institute of Physics, Chinese Academy of Sciences (1998). He became a special researcher at the National Institute for Materials Science (NIMS) in Japan. He and Prof. Yoshio Bando invented the carbon nanothermometer (Nature, **415**, 2002, 599) and obtained the 16th Tsukuba Prize in 2005, together with Prof. D. Golberg. In 2006, Dr. Gao accepted the professorship in HUST. In Nov. 2016, he was promoted to 2nd Grade Professor. He has published more than 135 peer-reviewed papers. His research interests include microstructure, energy devices and sensors based on nanomaterials.*

2. Theoretical research on TMDC heterostructures

The structure of monolayer TMDC involves a transition metal atomic layer sandwiching two chalcogen atomic-layers, in the cross-sectional view. TMDCs have two typical phases, 2H and 1T, which show the semiconductor properties and conductor properties, respectively. Their optical and electronic properties can be studied by first-principles calculation and scanning tunneling electron microscope (STM) technology. The structure construction of few-layer TMDC-based LEDs could be classified into metal–TMDC junctions like graphene/MoS_2, metal–insulator–TMDC structures like graphene/BN/WSe_2, and p–n junctions based on two TMDCs like MoS_2/WSe_2, or p–n junctions based on one TMDC with a wide-bandgap semiconductor like MoS_2/GaN, as shown in Fig. 1. The luminescence performances of TMDC-based LEDs are outlined, including, EL chromaticity, EQE, and polarization. Novel EL devices, including single-photon emitters, alternating voltage pulsed LED, and thermal light-emitting devices, will be reviewed in detail.

To gain insight into probable applications of TMDCs, it is essential to research their electronic properties such as the bandgap structure, carrier density, and carrier lifetime. According to the Bethe–Salpeter equation, the large difference in electron (m_e) and hole quality (m_h) leads to a small exciton binding energy, thus inducing good optoelectronic properties. The structural, electronic, and optical properties of $CsPbI_3$/MS_2 (M = Mo, W) heterostructures were investigated by density functional theory (Fig. 2a and b).[37] The differences between the conduction band minimums (conduction band offset, Δc) or valance band maximum (valence band offset, Δv) of the heterostructure are crucial for electron transport or hole blocking.[37] To obtain stable $CsPbI_3$/MS_2 heterostructures, the binding energies of $CsPbI_3$/MS_2 heterostructures were calculated using the formula below:

$$E_b = (E_{heterojunction} - E_{perovskite} - E_{MS_2})/N \quad (1)$$

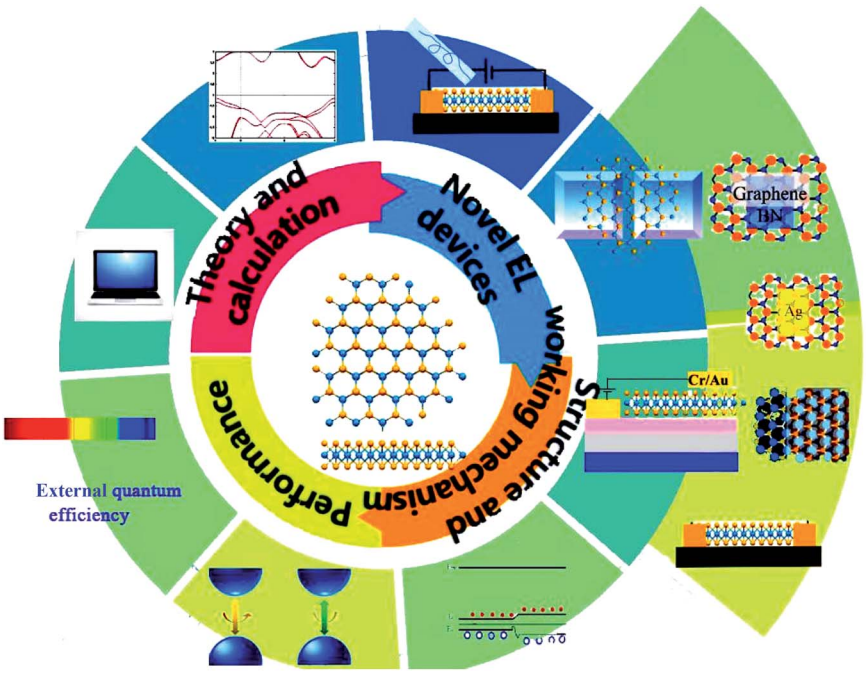

Fig. 1 The four aspects of light-emitting diodes (LED)-based on TMDCs, namely, theory and calculation, structure and working mechanism, performance, and novel electroluminescence devices. Direction I denotes the theoretical work of TMDCs, including the related semiconductor theory and density function theory calculation. Direction II denotes the structure and working mechanism of LEDs based on TMDCs, including the M–I–S junction, M–S junction, and p–n junction. Direction III denotes the performance of TMDCs-based LEDs, including polarity, color, and external quantum efficiency of the light emission. Direction IV denotes novel EL devices like thermal light-emitting devices and single photon emitters.

where $E_{\text{heterojunction}}$ represents the energies of heterostructures, $E_{\text{perovskite}}$ and E_{MS2} correspond to the energies of the isolated $CsPbI_3$ surface and monolayer MS_2, respectively. N denotes the interfacial area of $CsPbI_3/MS_2$ heterostructures. The charge density difference $\Delta\rho(Z)$ along the Z-direction was characterized as follows:

$$\Delta\rho(Z) = \rho(Z)_{\text{total}} - \rho(Z)_{\text{perovskite}} - \rho(Z)_{MS_2} \quad (2)$$

where $\rho(Z)_{\text{total}}$, $\rho(Z)_{\text{perovskite}}$, and $\rho(Z)_{MS_2}$ are the charge densities of the heterostructure, the isolated perovskite surface, and monolayer MS_2, respectively.

The electronic properties of TMDC LEDs can be mediated by the external electric field and external stress. Based on density functional theory, Li *et al.*[38] indicated that the electric field had little influence on the bandgap of the MoS_2 monolayer but it can adjust the charge transfer between the MoS_2 monolayer and the graphene substrate. Moreover, Hu *et al.*[39] proposed that the weak vertical electric field had little influence on the E_g of MoX_2, while the strong one could effectively achieve its modulation of E_g. The band gaps of monolayer $SnSe_2$ slightly increased with the in-plane tensile strains (Fig. 2c).[40] A semiconductor-to-metal transition at 10% strain was present for bilayer $SnSe_2$ (Fig. 2c).[40] The electrical field perpendicular to the bilayer SnS_2 and $SnSe_2$ modulated their electronic bandgap (Fig. 2d). The charge density difference and built-in electric field across the interface of TMDC van der Waals (vdWs) heterostructures prevent photogenerated electron–hole recombination, which goes against the light emission.[41] By using first-principles calculations, Zhang *et al.*[42] demonstrated that the $MoSe_2/WSe_2$ heterobilayer experienced transitions from type-II to type-I and then to type-II under various external electric fields perpendicular to the layers, which provides great application potential for ultrathin $MoSe_2/WSe_2$ heterostructures in future nano-devices and optoelectronics. As shown in Fig. 2e, the charge distribution can be controlled by an external electric field and the light emission properties will vary with the electronic properties (Fig. 2f).[43]

The light-emission properties of TMDCs can also be manipulated by the working temperature. Li *et al.*[43] investigated intralayer excited-state bi-excitons in graphene/WS_2 heterostructures. The binding energy and thermal activation energy of the excited-state biexcitons were obtained to be about 78 and 32 meV, respectively, by temperature-dependent PL intensity analysis, which was further confirmed by theoretical calculations using the stochastic variational method. The PL intensities of trions and bi-excitons as a function of the inverse of temperature were well fitted using the following thermal activation equation (solid lines):

$$I(T) = \frac{I_0}{1 + \left[A \exp\left(\frac{-E_B}{K_B T}\right)\right]} \quad (3)$$

where I_0, E_B, and k_B are the PL intensity at 0 K, the thermal activation energy, and the Boltzmann constant, respectively (Fig. 2g). The obtained thermal activation energies for trions and bi-excitons were 34 and 32 meV, respectively.[44]

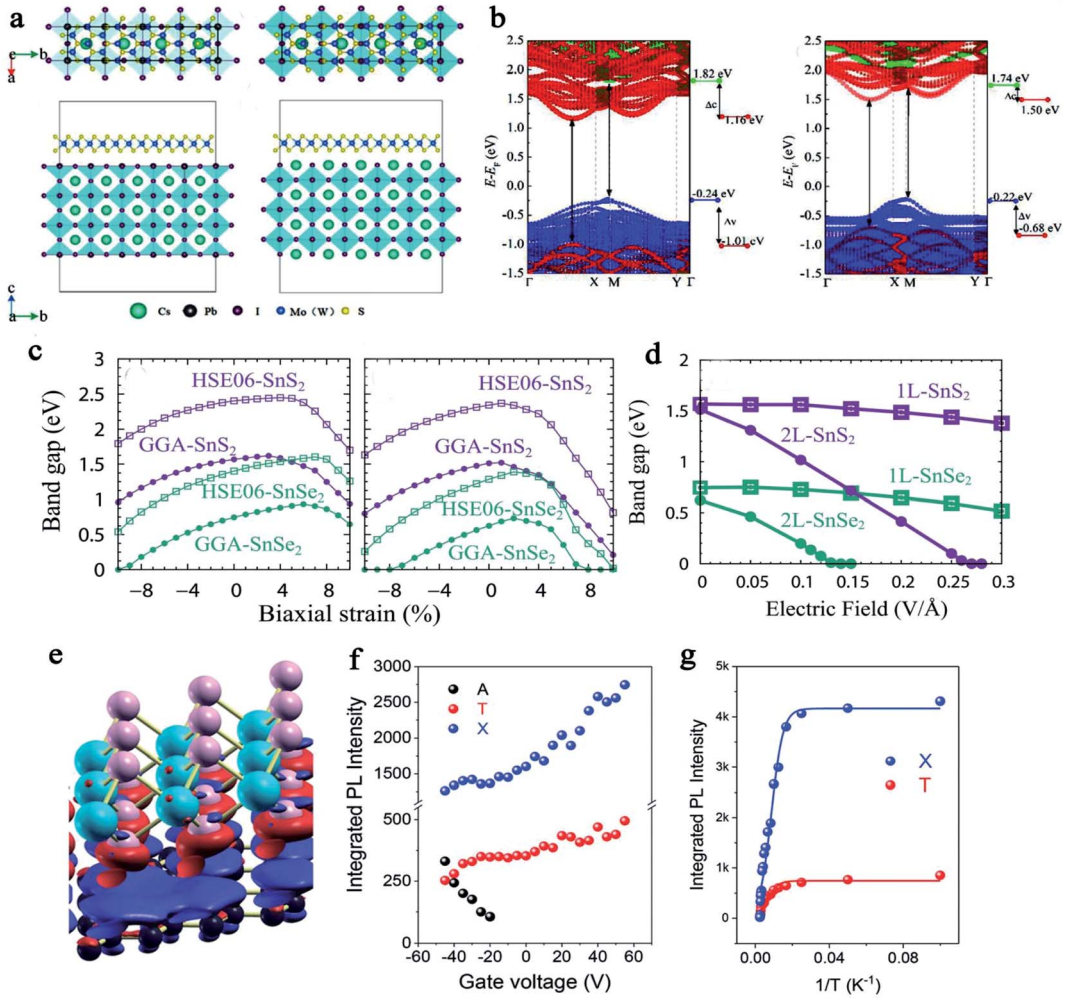

Fig. 2 (a) Top and side views of $CsPbI_3/MS_2$ (M = Mo, W) heterostructures with Pb–I termination (left panel); top and side views of $CsPbI_3/MS_2$ heterostructures with Cs–I termination (right panel). (b) Projected band structures of $CsPbI_3/MoS_2$ heterostructures with (left panel) Pb–I and (right panel) Cs–I terminations. Green, blue, red and dark yellow points represent the contributions of Pb, I, Mo (W), and S atoms, respectively. The short lines in the right planes are the band edges of the perovskite and MS_2 parts of the heterostructures. (a and b) Reproduced with permission;[37] Copyright 2019, American Chemical Society. (c) Variations of (left) the band gaps for monolayer SnS_2 and $SnSe_2$, (right) the band gaps for bilayer SnS_2 and $SnSe_2$ under biaxial compressive and tensile strains. (d) The variation of band gaps as a function of an applied electric field in a normal direction. (c and d) Reproduced with permission;[40] Copyright 2019, Elsevier. (e) Changes in the electronic charge densities. The red and blue isosurfaces correspond to charge increase and decrease, respectively. (f) Integrated PL intensity of excitonic emissions as a function of gate voltage. (g) Integrated PL intensity for X and T emissions as a function of inverse of temperature (1/T). (e–g) Reproduced with permission;[43] Copyright 2019, Royal Society of Chemistry.

3. The structure and working mechanism of TMDC-based LEDs

TMDC-based LEDs have been fabricated in a variety of refined structures, including metal–insulator–semiconductor (MIS) junction, p-type semiconductor/n-type semiconductor (p–n) junction,[29] metal–semiconductor (MS) junction.[45] Among these structures, the p–n junction of two TMDC layers or TMDC with other routine materials is the key.[46] For instance, Ghorai *et al.*[47] fabricated highly luminescent WS_2 quantum dots/ZnO heterojunction devices that emit white light.

3.1. MIS junction

TMDC LEDs based on MIS junctions have been extensively reported. Berraquero *et al.*[48] prepared a tunneling diode based on the vertical heterostructure of a single layer of graphene (SLG), hexagonal boron nitride (hBN) layer and a layered WSe_2 (Fig. 3a), a single quantum well structure. Without bias voltage between the SLG and the monolayer TMDC, the Fermi energy (E_F) of the system is constant across the heterojunction, keeping the net charge from flowing between the layers (Fig. 3b). With a negative bias, the E_F of SLG is raised above the minimum of the conduction band (E_C) of WSe_2. As a result, electrons tunnel from the SLG into the monolayer WSe_2, and then tunneling electrons recombine with holes in WSe_2 and release light (Fig. 3c). In the MIS junction, the injection of carriers into the semiconductor layer is unipolar.[45] A double quantum well structure was reported in another work.[49] Clark *et al.*[24] put forward the single-defect LED based on a vertical device constructed by two graphenes separated by WS_2 using layered

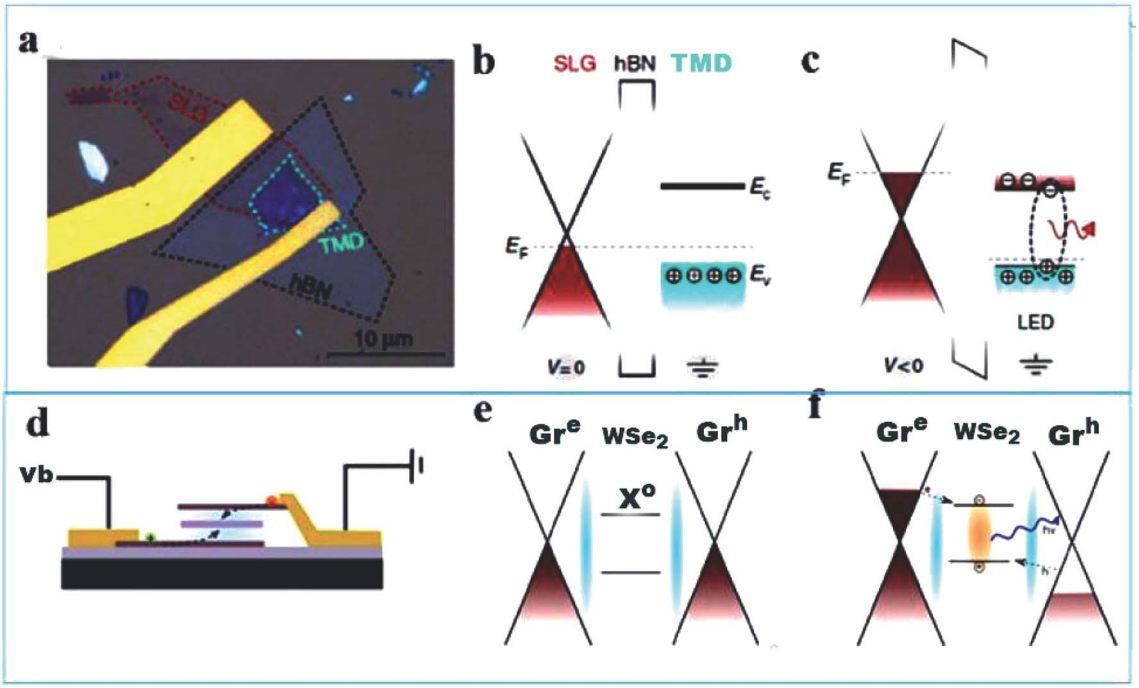

Fig. 3 (a) Optical microscope image of SLG/BN/WSe_2 LED. (b) Band diagram illustration of SLG/BN/WSe_2 LED under zero-applied bias. (c) Band diagram illustration of SLG/BN/WSe_2 LED under a finite negative bias. (a–c) Reproduced with permission;[48] Copyright 2016, Springer Nature. (d) The structure of graphene/WSe_2/graphene heterostructure LED. (e) The band diagram illustration of the device under zero-applied bias. (f) The working mechanization of the graphene/BN/WSe_2/BN/graphene heterostructure LED under the external bias. (d–f) Reproduced with permission;[24] Copyright 2016, American Chemical Society.

hexagonal boron nitride (BN) barriers (Fig. 3d–f). Liu *et al.*[50] fabricated the vertically assembled double quantum well structure LED using graphene/boron nitride as top and bottom tunneling contacts and monolayer WSe_2 as an active light emitter, which increased the probability of radiative recombination as compared to a single quantum well structure. They locally enhanced the EL by integrating a photonic crystal cavity on top of the heterojunction, as shown in Fig. 4a. The enhancement of EL can be attributed to the increase in the spontaneous emission rates of WSe_2 by the Purcell effect induced by the photonic crystal cavity.[50]

The aforementioned works are based on the vertical MIS structure. The following works are based on the paratactic MIS structure. Bie *et al.*[51] demonstrated the $MoTe_2$-based lateral junction with an electrostatic split-gate configuration integrated with a silicon photonic-crystal (PhC) waveguide, as shown in Fig. 4b. The structure can also be seen as the paralleling of two MIS junctions. Remarkably, the device had a grating coupler at the far end of the waveguide to allow excitation and collection.

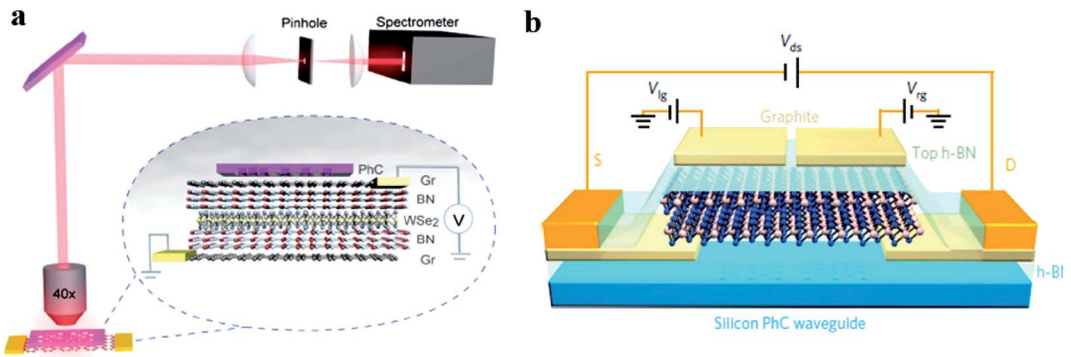

Fig. 4 Metal–insulator–semiconductor LED integrated with some kind of functional unit. (a) Schematic of light-emitting vdWs heterostructures of the graphene/boron nitride and its integration with a photonic crystal cavity and the EL measurement setup. Reproduced with permission;[50] Copyright 2017, American Chemical Society. (b) Schematic of the encapsulated bilayer $MoTe_2$ p–n junction on top of a silicon PhC waveguide. Reproduced with permission;[51] Copyright 2017, Springer Nature.

When the device works as an LED, the emitted light near the junction section couples to the waveguide, where it travels in-plane to the grating coupler. As a result, the light emission can be detected near the grating coupler. The integration of TMDC LED with a photonic-crystal provides an effective strategy for enhancing the EL intensity.

3.2. P–n junction (p–i–n junction)

The P–n junction is the most important LED structure. Two kinds of TMDCs can be fabricated as 2D–2D heterojunction diodes. With different band gaps of the p(n) type materials, the p–n junction LED can emit light of different colors.[28,52] In general, TMDC-based LEDs cannot emit light in the full visible light range due to the narrow bandgap. The injection of carriers into the semiconductor layer is a bipolar injection in the p–n junction LED.[45] Cheng *et al.*[53] created a p–n diode using the p-type monolayer tungsten diselenide (WSe_2) and n-type few-layer molybdenum disulfide (MoS_2) (Fig. 5a). As for the working mechanism of this LED, the conduction band of MoS_2 is below that of WSe_2, and the valence band of WSe_2 is below that of MoS_2. At a small bias voltage, holes can go across the junction, then inject into the MoS_2 region and recombine with the electrons, emitting light; the electrons cannot go across the junction (Fig. 5b). At a large bias, the conduction band in MoS_2 shifts upward and is higher than that in WSe_2; the electrons can go across and are injected into the p-WSe_2, while the holes can go across and are injected into the n-MoS_2 (Fig. 5c). Therefore, the light intensity undergoes a marked increase with more electron–hole recombination in both WSe_2 and MoS_2 regions. A scalable, two-step and *in situ* growth chemical vapor deposition strategy was employed to synthesize self-aligned WSe_2–MoS_2 monolayer lateral heterojunction arrays and demonstrate their LEDs.[54]

Superior to the heterojunction, the p–n homojunction exhibits ideal diode characteristics (Fig. 5d) because there is no potential discontinuity on the homojunction. In the heterojunction, the tip or notch between the conduction band and the valence band can result in carrier scattering and trap positions near the boundary surface. Jin *et al.*[55] proposed a p–n homojunction based on the p-type Nd-doped $MoSe_2$ and intrinsic n-$MoSe_2$ (Fig. 5e). When the Fermi level moves up at the positive V_g, this ideal diode behavior degenerates. In Fig. 5f, when $V_g > 0$ V, electron diffusion promotes the increase of the in-band composite current. They assumed that the Fermi levels of p-$MoSe_2$ and n-$MoSe_2$ moved upward with the same energy through the V_g bias.[55] Li *et al.*[56] fabricated the MoS_2 p–n homojunction by spin-coating $AuCl_3$ and benzyl viologen on

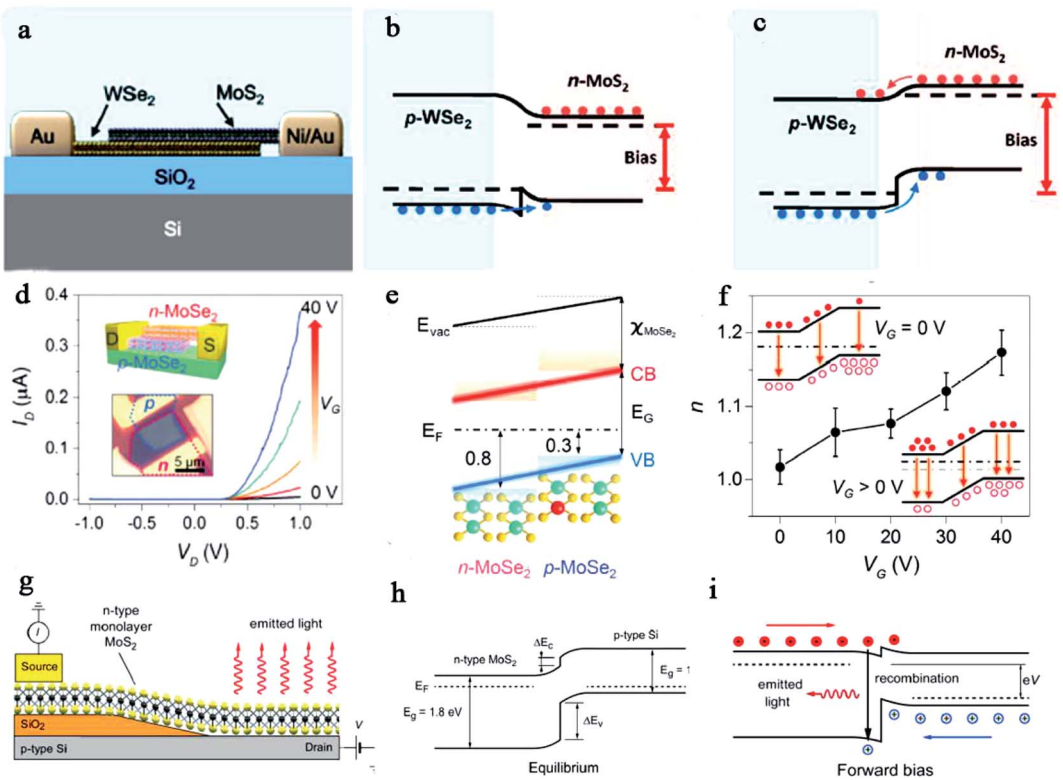

Fig. 5 Schematic illustration and band diagram of a p–n heterojunction diode. (a) The cross-sectional schematic illustration of the WSe_2/MoS_2 heterojunction. (b) The ideal band diagram of the WSe_2/MoS_2 heterojunction under a small forward bias, and (c) under a large forward bias. (a–c) Reproduced with permission;[53] Copyright 2014, American Chemical Society. (d) V_G-dependent rectifying behavior of the $MoSe_2$ homojunction p–n diode. (e) Energy bandgap schematic for the $MoSe_2$ homojunction. (f) Ideality factor of the $MoSe_2$ homojunction as a function of gate bias. (d–f) Reproduced with permission;[55] Copyright 2015, WILEY-VCH. (g) The cross-sectional view of the structure of the MoS_2/Si heterojunction LED. (h) Band diagram of the MoS_2/Si heterojunction in equilibrium conditions and (i) under forward bias. (h and i) Reproduced with permission; Copyright 2014, American Chemical Society.[57]

MoS_2 with post-annealing, respectively. The ultimate thickness of the MoS_2 vertical homojunction is 3 nm and the depth of chemical doping is 1.5 nm.

To expand the application range of TMDC LEDs, 2D/3D heterojunction diodes based on TMDC in contact with wide band-gap bulk materials were developed. Lopez-Sanchez *et al.*[57] studied vertical heterojunctions composed of n-type monolayer MoS_2 and p-type silicon (Fig. 5g). Because of the difference in electron affinity and bandgap between Si and MoS_2, the junction has the characteristics of conduction ($\delta E_c = 200$ meV) and valence state band shifts ($\delta E_v = 900$ meV) (Fig. 5h). Under forward bias to the heterojunction, electrons from the n-MoS_2 side and holes from p-Si can radiatively recombine in the junction, resulting in light emission. For the valence band and conduction band offset, the valence band and conduction band tip will affect the charge carrier injection efficiency and limit the device current (Fig. 5i). The tunneling diode (p–i–n) composed of a vertical $MoS_2/SiO_2/Si$ heterostructure was also demonstrated.[58] The ionic-liquid gated light-emitting transistor was fabricated on WS_2 monolayer and bilayers.[59] For TMDCs, the p–n junction can be divided into two kinds: the first one is the vertical p–n junction, which shows large EL intensity for large junction area; the second one is the lateral p–n junction, which shows weaker EL intensity for relatively smaller junction area.

The field-induced p–n junction is an important atomic p–n junction because TMDC possesses atomic thickness and has the potential to be used in microelectronics. Electric field-induced p–n junctions can be used to realize peculiar functionalities in TMDC materials, for which the conventional chemical doping method is difficult to achieve. The field-induced p–n junctions play crucial roles in realizing LED operations as well as circularly polarized EL. Zhang *et al.*[60] fabricated electric field-induced p–n junction and demonstrated that the built-in potential became negative under a forward bias voltage. Baugher *et al.*[61] constructed LEDs based on the field-induced p–n diode on monolayer WSe_2. Yumin *et al.*[62] prepared an anion-induced p–n junction based on a WS_2/boron nitride heterostructure, which is another method for creating p–n junctions. A 0D–3D p–n diode composed of MoS_2 quantum dots and Si was also fabricated to exhibit white light emission from ~450 nm to 800 nm under forward bias.[63] The construction of mixed-dimensional van der Waals heterostructures can take advantage of the different dimensional properties to produce devices with novel functionalities.

3.3. M–S junction

Another type of TMDC LED is based on the M–S junction, which is also called the Schottky diode. Lien *et al.*[64] created an AC voltage pulsed LED based on the Schottky diode of the TMDC monolayer/Au junction. Puchert *et al.*[65] focused on broadband silver EL in Ag/MoS_2 nano-LEDs. Due to the low luminescence efficiency of TMDCs LED, several studies were devoted to enhancing the light-emitting performance. Hole injection into the single-layer WSe_2 was enhanced by incorporating a metal contact and the EL was enhanced.[66] To optimize the device performance of LEDs, the solution-processed MoS_2 was used as a hole-injecting electrode, and an electron blocking layer in the form of MoO_3 was fabricated.[67] A visible organic LED was fabricated using tris(8-hydroxy-quinolinato)aluminum as the emissive layer and MoS_2 + PEDOT:PSS as the hole-injection layer, emitting 375 nm electroluminescence with high efficiencies of 8.1 cd A^{-1} and 5.7 lm W^{-1}.[68]

4. Luminescence properties of TMDC LEDs

4.1. EL peak location and origin

The luminescence properties of LEDs cover parameters such as EL peak location, EQE, International Lighting Commission chromaticity coordinates (CIE 1931 color diagram), EL polarization, rectifying characteristics, ideality factor, and the switching ratio of the LED p–n junction. The luminescence properties of few-layer TMDC LEDs are reviewed as follows.

Generally, EL is related to the energy bandgap of TMDCs. Light of long wavelength results from narrow bandgap characteristics, and broad bandgap emission will bring out short wavelength light. The EL of TMDC LEDs varies from infrared to green light. The EL peaks of TMDC LEDs are often compared with the PL peak to ascertain the origin.[69] In layered TMDCs, the EL is primarily attributed to intrinsic excitons (X^o), charged excitons or trions (X^+/X^-), free-space emission, and defect-trapped excitons. It is necessary to note that white light emission can be achieved in TMDC-based LEDs by combining TMDC with a broad bandgap semiconductor.

2Monolayer TMDCs can emit light in a highly efficient manner despite being sub-nanometers thick.[70] Ross *et al.*[69] observed the EL of a WSe_2 monolayer p–n junction at an injection current as low as 200 pA; the EL and PL peaks were consistently located at 1.65 eV (red light) (Fig. 6a). This PL peak is the natural result of the large exciton binding energy of monolayer TMDC due to strong Coulomb interactions, which indicates that in the EL mechanism, the injected electrons and holes form excitons before radiative recombination (Fig. 6b).[71,72] With the increase in the injected current, the EL emission intensity increased until it was beyond 2 mA. This is related to the heating effect of the device. Ghorai *et al.*[47] fabricated light-emitting devices of highly luminescent WS_2 quantum dots/ZnO heterojunctions (Fig. 6c). Under the injection current of 1.4 mA, the deconvolution of the wide EL spectrum showed three different emission peaks at about 450 nm, 505 nm, and 597 nm. The first peak is the characteristic emission of WS_2 nanocrystals, the remaining two peaks are from the emission of defect-related excitons in ZnO (Fig. 6d). Ye *et al.*[73] identified the direct-exciton and bound-exciton recombination process in MoS_2/Si LED. The auger recombination of the exciton–exciton annihilation of bound exciton emission was observed.[73] Sundaram *et al.*[74] measured the EL of monolayer MoS_2 field-effect transistors (Fig. 6e), which showed a peak at ~685 nm, matching well with the PL peak at ~680 nm; therefore the EL and PL of that device involved the same excited state, the B exciton (Fig. 6f).

Importantly, temperature-dependent PL measurements can be used to profoundly probe the EL peak origin. Yang *et al.*[75] measured the EL from the p-Si/i-WS_2/n-ITO heterojunction at 77

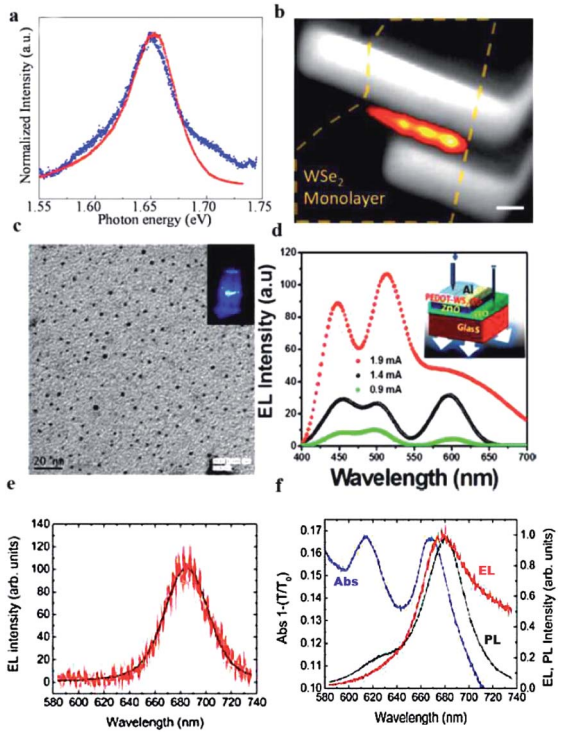

Fig. 6 The PL and EL spectral contrast of TMDC-based LEDs in search of the EL peak origin. (a) At 300 K, the EL spectrum (blue) of the monolayer WSe_2 p–n junction generated by a current of 5 nA closely resembles the PL spectrum (red). (b) The EL image (red) superimposed on the WSe_2 p–n junction device image (grayscale). (a and b) Reproduced with permission;[69] Copyright 2014, Springer Nature. (c) The TEM images of the as-synthesized WS_2 nanocrystals. Inset is the photo of WS_2 nanocrystals suspended in DMF. (d) EL spectra of the Al/PEDOT-PSS/WS_2/ZnO/ITO device under different applied currents. Reproduced with permission;[47] Copyright 2017, American Chemical Society. (e) EL spectrum of a 1L-MoS_2 field effect transistor measured at $V_D = 5$ V and $I_D = 100$ μA. (f) Absorption (Abs), EL, and PL spectra on the same 1L-MoS_2. The EL spectrum was measured at $V_D = 8$ V and $I_D = 164$ μA. Reproduced with permission;[74] Copyright 2013, American Chemical Society.

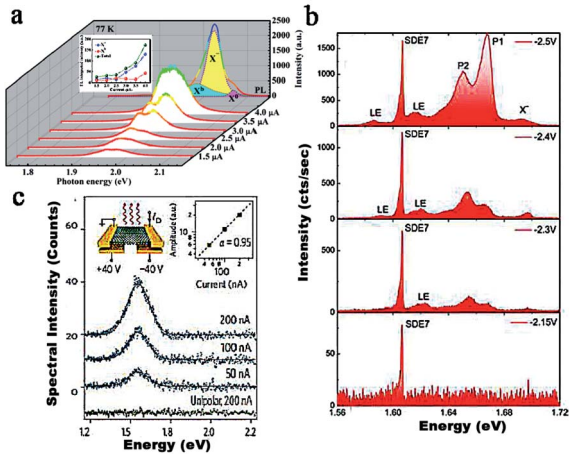

Fig. 7 Current-dependent EL and temperature-dependent PL spectra of the LED device. (a) EL spectra of the LED device recorded at 77 K under different injection currents. Reproduced with permission;[75] Copyright 2016, American Chemical Society. (b) Evolution of EL spectra under different bias. Labels SDE1 and LE are used to denote the EL peaks of the single-defect emitters and other localized states, respectively. Reproduced with permission;[77] Copyright 2014, American Association for the Advancement of Science. (c) EL emission spectra of the monolayer WSe_2 p–n junction recorded for gate voltages. Reproduced with permission;[78] Copyright 2014, Springer Nature.

K; two main emission peaks at 1.950 and 1.985 eV (red light) were detected, as shown in Fig. 7a. A temperature-dependent PL measurement had also been carried out in the temperature range from 81 K to 294 K to trace the emission peaks. The energy of emission peak located at 1.950 and 1.985 eV (red light) matched well with the observed X^b (defect-induced bound exciton) and X^- (trion) in the PL spectra at low temperature.[75] Multilayer WSe_2 emits light more easily than monolayer WSe_2 due to its larger light density.[76] Schwarz *et al.*[77] measured the typical EL spectra of a single-defect emitter under different applied voltages. A single sharp line at 1.607 eV, labeled SDE1, from the single-defect emitter (SDE) dominated the EL spectrum (Fig. 7b). As shown in Fig. 7c, Pospischil *et al.*[78] showed the EL emission peaks at 1.547 eV of the gate-split WSe_2 monolayer LED, which was 93 meV below of PL peak of monolayer WSe_2 in energy. The peak shift was assigned to different dielectric environments in both experiments, which influenced the exciton bound energy due to Coulomb screening. In addition, light emission from high-order correlated exciton states was reported in the hBN-encapsulated monolayer WSe_2 and WS_2 upon bias voltage excitation. The EL was from charged biexcitons and dark excitons.[79]

4.1.1. Visible light LED. Highly efficient visible light emission is significant for TMDC-based LEDs. Many methods have been adopted to improve the EL of layered TMDC LEDs.[23,70,80] Yumin *et al.*[62] realized orange light emission centered at 620 nm from anion induced p–n junction of a WS_2/boron nitride heterostructure (Fig. 8a–c). Perumal *et al.*[81] achieved red light from a single layer n-MoS_2/SiO_2/p-GaN heterostructure device. Chen *et al.*[82] designed an ultrathin $MoSe_2$/GaN heterojunction diode, demonstrating high-intensity EL at 407 nm (violet light) and ~850 nm (infrared light) (Fig. 8d and e). Ke *et al.*[15] prepared the enhanced EL of CdSe quantum dots coupled with MoS_2–chitosan nanosheets. Nikam *et al.*[83] observed white-light-emitting constituents of the p-GaN/p-MoS_2/n-MoS_2 heterostructure, whose EL spectra consisted of three emission peaks of ~481 nm (blue light), ~525 nm (green light), and ~642 nm (orange light). The device showed the white color purity of CIE (0.41, 0.41). Andrzejewski *et al.*[84] reported red light LED, which was fabricated by embedding a metal–organic (MO-)CVD WS_2 monolayer into a vertical p–i–n device architecture of organic and inorganic injection layers. The multicolor LED can be fabricated based on MoS_2 QD, and the emission wavelength can be tuned from blue to red by adjusting the thickness of the QD layers.[21] The representative visible light LEDs are summarized in Table 1.

4.1.2. Infrared light LED. Infrared light LEDs based on TMDCs are easy to construct. The infrared EL peak often originates from direct transitions in monolayer TMDCs or indirect transitions in multilayer TMDCs. Bie *et al.*[51] fabricated a red light LED of the $MoTe_2$ p–n junction, which realized the EL peak of

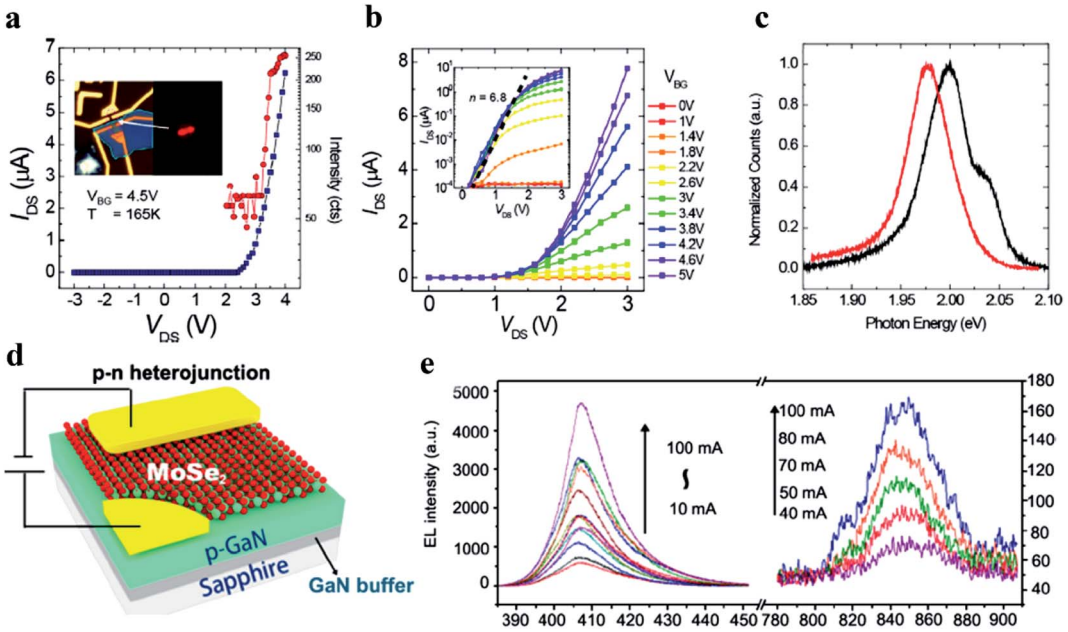

Fig. 8 The visible light emission of TMDCs-based LEDs. (a) The electrical performance of the TMDCs/boron nitride (BN) heterostructures device under a 4.5 V backgate voltage and 5 V liquid gate voltage at a temperature of 165 K. (b) Electrical properties of the TMDs/boron nitride (BN) heterostructure device under different backgate conditions at 80 K. (c) EL (red) and PL (black) spectra at 80 K under 650 mW m^{-2} fluence power. (a–c) Reproduced with permission;[62] Copyright 2017, John Wiley and Sons. (d) Schematic of the device consisting of an atomic $MoSe_2$ layer on a p-type GaN/sapphire substrate. (e) EL spectra of the n-$MoSe_2$/p-GaN device in the short- and long-wavelength regions. Reproduced with permission;[82] Copyright 2016, American Chemical Society.

1090 nm and 1175 nm at cryogenic and room temperatures, respectively. The peaks were due to intrinsic excitons (X^o) of bilayer $MoTe_2$. Both PL and EL peaks demonstrated red shifts at higher recording temperatures (Fig. 9a). The excitonic (X^o) and trionic (X^+) peaks can be clearly distinguished in the PL map (Fig. 9b). Moreover, as seen in Fig. 9c, a narrow peak at 1160 nm was on top of a broader peak centered at 1175 nm. The 1160 nm peak was due to the photonic crystal mode, and the 1175 nm peak matched the free-space emission of the bilayer $MoTe_2$. Ponomarev *et al.*[85] found EL in the ionic liquid field-effect transistor based on monolayer MoS_2, as shown on the right side of Fig. 9d. The free exciton peak at 660 nm and an additional EL peak were found, as seen in Fig. 9e and f. The additional EL peak was due to the presence of defect states at an energy of 250–300 meV above the top of the valence band, acting as deep traps for holes. Cheng *et al.*[53] found infrared light emission near 880 nm, which was due to the indirect bandgap transition in bilayer WSe_2. Interestingly, a significant direct bandgap exciton emission was found in the EL of multilayer MoS_2.[86] The detection of the 1034.6 nm single EL peak in monolayer $MoTe_2$ LED indicated that the monolayer $MoTe_2$ maintained a high quality after the device fabrication process (Fig. 9g and h).[87] The EQE is related to the current injection efficiency (Fig. 9i). A 2D–1D heterostructure of p-type MoS_2 nanosheets and n-type CdSe NW was fabricated as an LED, exhibiting electroluminescence at 709 nm.[88] Zheng *et al.*[89] found an infrared cathodoluminescence (CL) peak near 1.572 eV *via* the hBN/WSe_2/hBN heterostructure, which corresponded to the exciton energy of monolayer WSe_2. The CL of TMDCs has been found by sandwiching between two hBN layers, but the CL of TMDCs was scarcely found by the direct

Table 1 The structure composition and luminescence wavelength of visible light light-emitting diodes based on TMDCs

Structure composition	Peak position (nm)	Peak color	Peak origin
$MoSe_2$/GaN[82]	407	Violet	GaN
	850	Infrared	$MoSe_2$
P-GaN/p-MoS_2/n-MoS_2 (ref. 83)	481	Blue	GaN
	525	Green	P–MoS_2
	642	Orange	N-MoS_2
PEDOT:Poly-PD/WS_2/ZnO[84]	650–670	Red	WS_2
WS_2 quantum dots/ZnO[47]	450	Violet	WS_2
	505	Green	ZnO
	597	Yellow	ZnO
MoS_2 QD[21]	470–680	Full visible spectrum	MoS_2

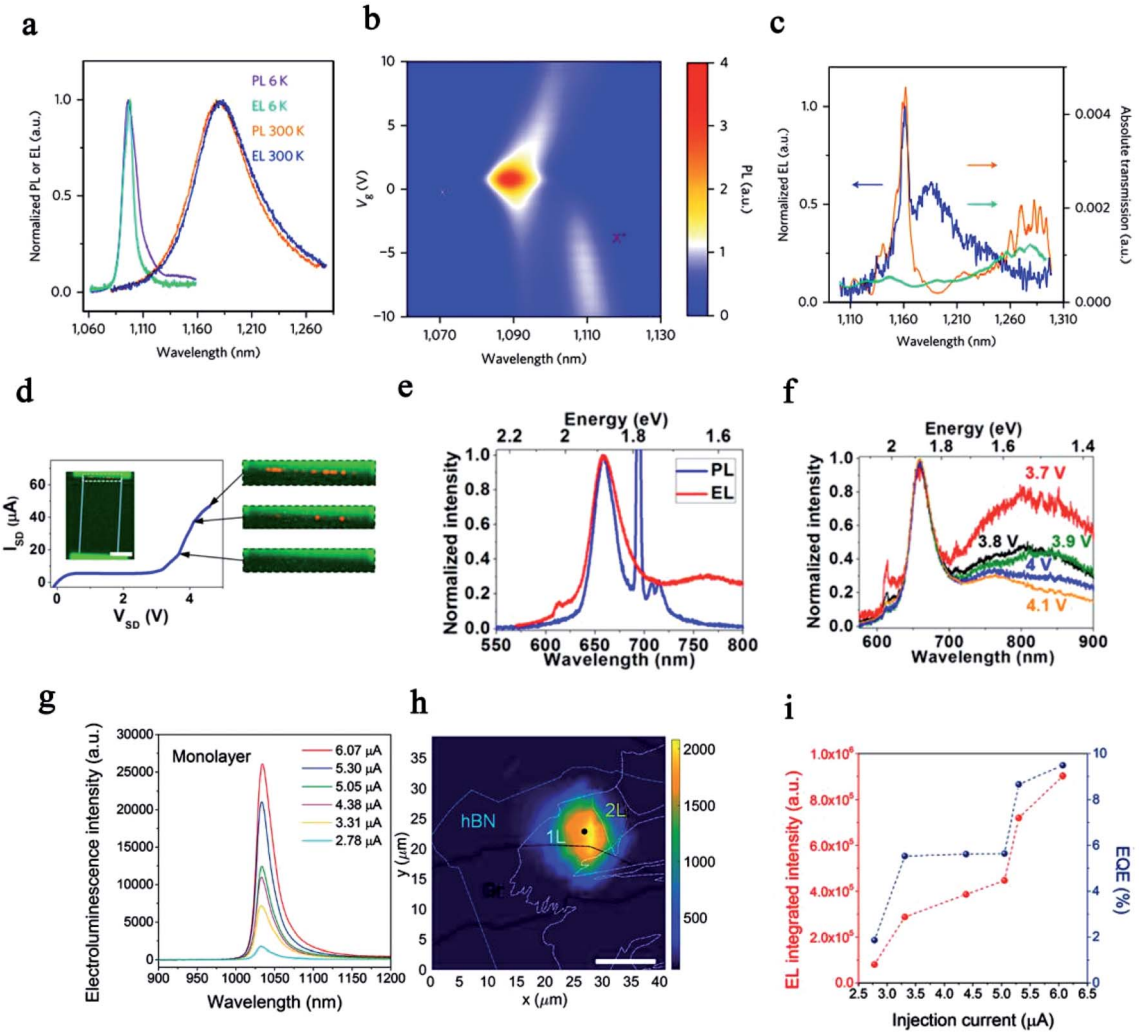

Fig. 9 PL and EL comparison of TMDCs LED. (a) PL and EL spectra of the bilayer $MoTe_2$ flake (the $MoTe_2$ p–n junction) at room temperature and at 6 K. (b) Spectrally resolved PL map of the bilayer $MoTe_2$ at 6 K as a function of gate voltage $V_g = V_{lg} = V_{rg}$. (c) EL and transmission of the waveguide before (orange) and after (green) transfer of $MoTe_2$. (a–c) Reproduced with permission;[51] Copyright 2017, Springer Nature. (d) Source–drain current I_{SD} as a function of source–drain bias extending to large V_{SD} values. The inset shows an image of the device with the region of the channel close to the hole injecting contact, where light emission occurs. (e) Comparison of the PL (blue curve) and EL (red curve) spectra ($V_{SD} = 4.1$ V) measured in the MoS_2-based ionic liquid field transistor. (f) Normalized EL spectra recorded for different values of source–drain bias V_{SD}. (d–f) Reproduced with permission;[85] Copyright 2015, American Chemical Society. (g) EL spectra from the hBN/monolayer $MoTe_2$/graphite LED under −20 V back gate voltage at 83 K. (h) EL mapping image of the $MoTe_2$ LED device under back gate voltage of −20 V. (i) EL intensity (left) and EQE (right) of monolayer $MoTe_2$ as a function of the injection current. (g–i) Reproduced with permission;[87] Copyright 2018, American Chemical Society.

measurement of TMDC materials. It can be concluded that it is still challenging to detect the interband CL signal in monolayer TMDCs, as the electron–hole creation cross-section is extremely small and only a small amount of recombination takes place in the top of the two-dimensional material, most of which takes place in the supporting slab.[89] There have been no recent reports on layered TMDC LEDs emitting ultra-violet light, so this may be a problem that needs to be solved.

4.2. Polarization electroluminescence

Circularly polarized light is involved in various fields ranging from 3D displays to spin sources in spintronics, and information carriers in quantum computation.[90,91] There is a strong demand for compact circularly polarized light sources to achieve high integration and controllable polarization.[92] Zhang *et al.*[92] first demonstrated WSe_2-based ambipolar transistors emitting circularly polarized EL (Fig. 10a). As shown in Fig. 10b–d, the degree of circular polarization EL from the p-Si/i-WS_2/n-ITO heterojunction LED device can be modulated simply by the injection current.[75] The excitons in monolayer WSe_2 forming in the ±K valleys were demonstrated using polarization-resolved PL.[69] The excellent matching of the EL peak with the PL peak thus proves that the EL also comes from such valley excitons. The injected electrons and holes form excitons in two valleys, thus producing unpolarized light, as shown in Fig. 10e.[75] Zhang *et al.*[60] realized bias voltage-

dependent circular polarization in an ionic liquid-gated field effect transistor of a bilayer WSe_2 thin flake, as seen in Fig. 10f and g, which possesses a peculiar valleytronic functionality through field-induced WSe_2 p–n junction. Ye *et al.*[93] demonstrated the electrically tunable valley polarization in the experiment. By accessing the extra spin degree of freedom (DOF) in electronics, spintronics can be applied for information processes, such as magnetoresistive random-access memory. To realize its potential in electronics, it is necessary to electrically control the valley DOF. These results are not only extremely interesting in physics but could also lead to many practical applications.[94]

4.3. Ideality factor

Clear current rectification behavior was observed for the WSe_2/MoS_2 heterojunction (Fig. 11a).[53] The ideality factor of the heterojunction device was calculated based on the model of a p–n diode being in series with a resistor (Fig. 11b). In the same heterojunction, the ideality factor of 1.2 was derived with a series resistance of 80 MΩ, at zero gate voltage, but the ideality factor of 3 was derived with a series resistance of 33 MΩ, at −20 V gate voltage.[53] The *I*–*V* characteristics were evaluated to extract the diode parameters including the reverse saturation current I_s and the ideality factor n of diodes by the following formula:

$$I = I_s\left(e^{\frac{qV}{nkT}} - 1\right) \tag{4}$$

where I_s is the saturation current derived from the straight line intercept of ln I at $V = 0$, as seen in Fig. 11c. q is the electronic charge, V is the applied voltage across the device, n is the diode ideality factor, k is Boltzmann's constant, and T is the absolute temperature.[95] From eqn (4), the ideality factor n can be given as

$$n = \frac{q}{kT}\left(\frac{\mathrm{d}V}{\mathrm{d}\ln I}\right) = \frac{q}{kT} \times \frac{1}{\text{slope}} \tag{5}$$

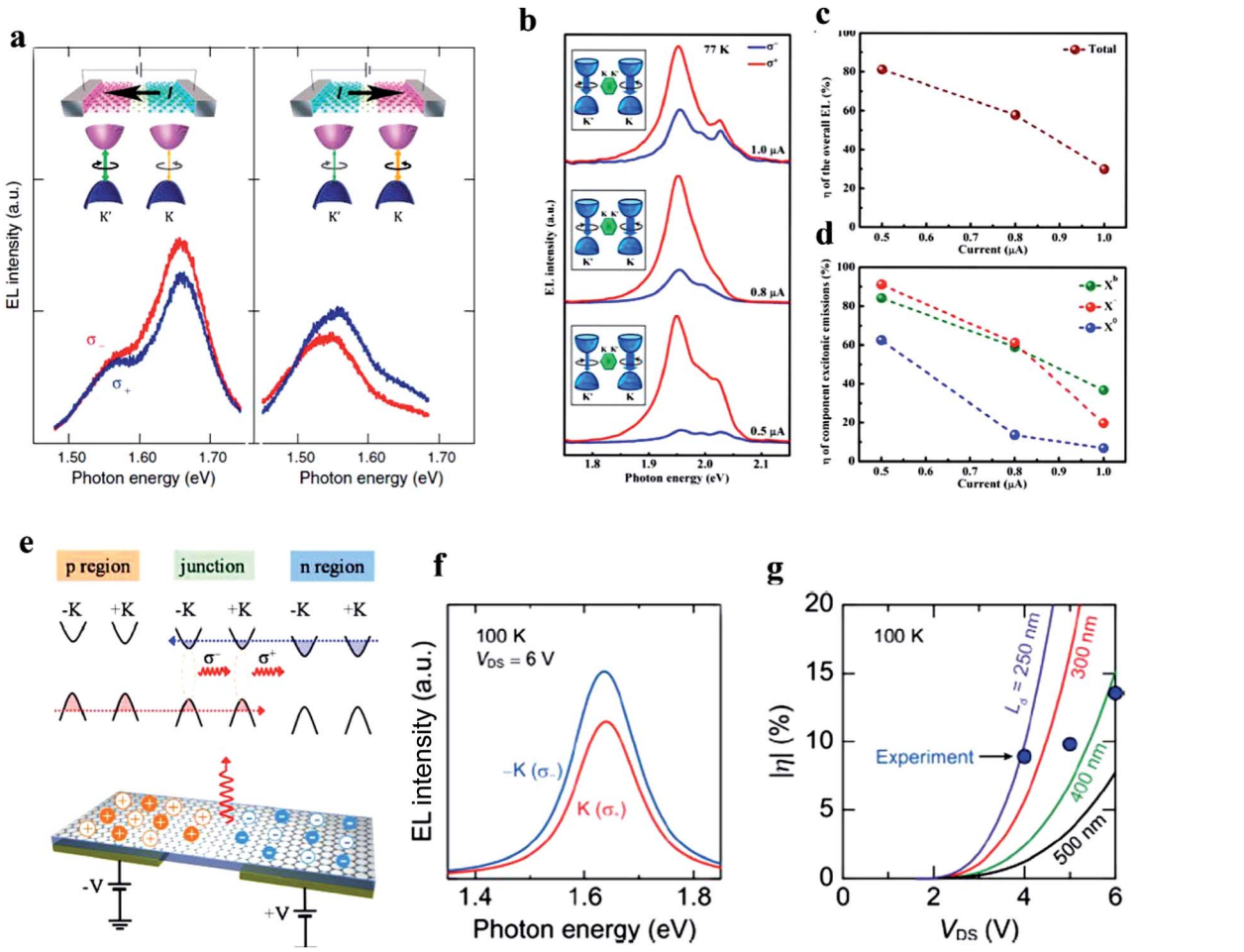

Fig. 10 Polarization electroluminescence (EL). (a) Circularly polarized EL spectra from p-Si/i-WS_2/n-ITO heterojunction ambipolar transistors for two opposite current directions. Reproduced with permission;[92] Copyright 2014, American Association for the Advancement of Science. (b) The current-dependent circularly polarized EL spectra from CVD-grown monolayer WS_2. (c) Current-dependence of the degree of circularly polarized EL for the overall emission and (d) component neutral excitons X^o, negative trions X^-, and bound excitons X^b. (b-d) Reproduced with permission;[75] Copyright 2016, American Chemical Society. (e) Band diagram and device schematic of EL generation from valley excitons. Reproduced with permission;[69] Copyright 2014, Springer, Nature. (f) Simulated polarized EL spectra from the WSe_2 p–n junction. (g) Bias voltage-dependence of the degree of circular polarization in the EL of the WSe_2 p–n junction. (f and g) Reproduced with permission;[60] Copyright 2017, American Chemical Society.

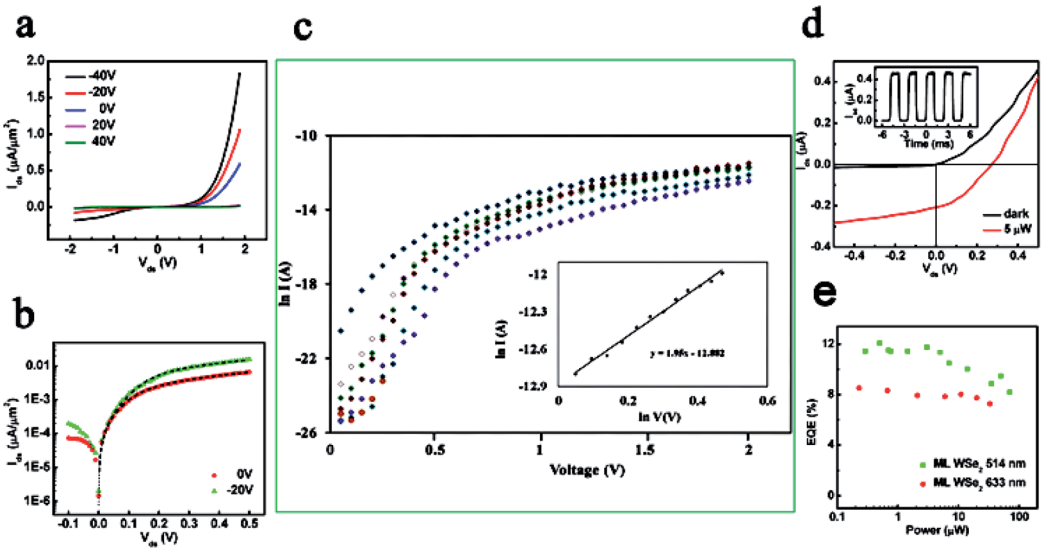

Fig. 11 (a) Gate-tunable output characteristics of the WSe_2/MoS_2 heterojunction p–n diode. (b) The ideality factor of the WSe_2/MoS_2 p–n diode. An ideality factor of 1.2 with a series resistor of 80 MΩ derived at 0 V gate voltage (red circle), and an ideality factor of 1.3 with a series resistor of 33 MΩ was derived at −20 V gate voltage (green triangle). (c) The forward semi-logarithmic *I*–*V* relation for the p-Si/n-WS_2 heterojunction diode at different thicknesses. The inset shows the ln *I* *vs.* ln *V* plot in the forward region. (c) Reproduced with permission;[94] Copyright 2017, Springer Nature. (d) Experimental output (I_{ds}–V_{ds}) characteristic of the vertical heterojunction device in the dark (black) and under the illumination of a laser at wavelength 514 nm with power of 5 mW. The inset denotes the temporal response of the photocurrent generation under 514 nm illumination (10 μW). (e) Power-dependent EQE of the heterojunction device under laser excitation at 514 and 633 nm, at $V_{DS} = 0$ V and $V_{BG} = 0$ V. A maximum EQE of 12% was observed. (a, b, d and e) Reproduced with permission;[53] Copyright 2014, American Chemical Society.

Notably, if $n \approx 1.0$, the diode must have ideal diode behavior. This characteristic is due to low charge trap density at the homojunction interface. An ideality factor greater than a unit represents a low-quality connection and is considered a sign of recombination loss.[96,97]

Kapatel *et al.*[95] studied layer-engineered *I*–*V* characteristics of the Si/WS_2 van der Waals heterostructure diode. In the 10 μm-thickness WS_2 diode, the ideality factor was 2 and the reverse saturated current was 5×10^{-10} A. In terms of the ideality factor, without laser illumination (514 nm, 5 μW) the electronic properties of an ideal diode are much better as compared to homojunction p–n diodes in TMDCs ($n \approx 1.6$).[56] The output characteristics (I_{ds}–V_{ds}) of the vertical heterojunction with the photovoltaic effect are shown in Fig. 11d. The ideality factor of the current–voltage was 1.64 for the homostructured WSe_2 rectifying diode.[98]

4.4. External quantum efficiency (EQE)

A series of work has been done on the improvement of the QY of TMDC photoluminescence (PL) and the EQE of TMDC LEDs.[39,99] Monolayer TMDCs usually experience low QY because of the high density of lattice defects. It is advantageous to increase the QY by overcoming the lattice defects. Unlike conventional semiconductors, the thermal treatment of TMDCs cannot repair the defect but the acid treatment can effectively repair the chalcogen vacancy defect.[100] The strong inter-exciton interactions in 1L-TMDCs were considered to be the primary limiting factor of QY.[29,101] The strong coulombic interactions between excitons induced an exciton–exciton annihilation (EEA) effect, in which excitons decayed in a nonradiative way.[29] Therefore, the density of radiative excitons was reduced. For photodetectors, the photo-to-electronic conversion efficiency is defined as the ratio of the number of carriers collected by electrodes to the number of incident photons.[53] The EQE in a MoS_2/WSe_2 vertical heterojunction can reach 11% under 514 nm laser excitation with a power of 5 μW (Fig. 11e).

For LEDs, the EQE can be evaluated from the ratio of collected EL photon number per second to the injected electron number. The internal quantum efficiency (IQE, η_{int}) and EQE (η_{ext}) can be calculated using the following equation:

$$\eta_{int} = \frac{P_{int}/hv}{I/e} \quad (6)$$

$$\eta_{extraction} = \frac{P/hv}{p_{int}/hv} \quad (7)$$

$$\eta_{ext} = \frac{P/hv}{I/e} = \eta_{int}\eta_{extraction} \quad (8)$$

where P_{int} denotes the optical power emitted from the active region and can be simplified to the number of photons emitted from the active region per second. P denotes the optical power emitted into free space and can be simplified to the number of photons emitted into free space per second. *I* denotes the injection current and can be simplified to the number of electrons injected into the LED per second.[87] η_{ext} denotes the extraction efficiency or external quantum efficiency, and can be an indicator of the limitations of high-performance LEDs; it is often lower than 50%. To date, the EQE of LEDs based on

Table 2 Summary of performance of layered TMDCs LED, in terms of material configuration, EL peak position, ideality factor, and external quantum efficiency (EQE)

Material configuration	EL peak position	Origin of peak	Ideal factor	EQE	Literature
P^+-Si/i-WS_2/n-ITO	1.950 and 1.985 eV	Bound exciton and trion peak of WS_2	—	—	Yang *et al.*[73]
Bilayer $MoTe_2$–silicon	1175 nm/1160 nm	Free-space emission of the bilayer $MoTe_2$/photonic crystal mode	—	0.5% at 1160 nm	Bie *et al.*[52]
Graphene/hBN/$MoTe_2$	1034.6 nm	Exciton of $MoTe_2$		9.5% at 83 K	Zhu *et al.*[85]
P-Monolayer WSe_2/n-MoS_2 junction	A (792 nm) and B (626 nm)	Exciton of WSe_2 and exciton of MoS_2	1.2	A maximum of 12%, 0.5 μW	Li *et al.*[56]
	A′ (546 nm) and B′ (483 nm)	Hot electron peak			
	I (880 nm)	Indirect band gap emission			
Graphene/BN/WSe_2/BN/graphene	1.651–1.71 eV (621–598 nm)	Defect-bound excitons	—	—	Clark *et al.*[24]
	1.72 and 1.75 eV (595–585 nm)	Charged and neutral intrinsic excitons			
Monolayer WSe_2 p–n junction	1.69 eV (606 nm)	X^0 recombination	—	IQE = 5%	Ross *et al.*[67]
	1.663 eV to 1.625 eV	X^- trion (two electrons and one hole)			
	1.670 eV (613 nm)	X^+ trion (two holes and one electron)			
	1.59 eV (644 nm)	Impurity-bound excitons (X^I)			
N–MoS_2/p-Si	694 nm	Intrinsic peak of MoS_2	—	4.4%	Sanchez *et al.*[58]
	644 nm	The heterojunction region			
	721 nm	Trion resonance of MoS_2			
Mono- and bilayer WS_2 ionic liquid gated FETs	1.95 eV (525 nm)	Direct transition	—	—	Jo *et al.*[97]
	1.7 eV (602 nm)	Indirect transition			
Monolayer WSe_2 p–n junction	752 nm	Direct-gap exciton transition	1.9	0.2% at 522 nm	Baugher *et al.*[55]
Graphene/BN/WSe_2/BN/Graphene	738.7 nm	X^0 recombination	1.14	Below 0.2%	Liu *et al.*[50]
	759 nm	X^-/X^+ impurity exciton peak			

TMDCs is relatively low.[51,53] The maximum EQE of 12% was achieved in the monolayer WSe_2/MoS_2 p–n diode.[50] The EQE reached 9.5% from LED on the graphene–hBN–$MoTe_2$ heterostructure.[87] The EQE of MoS_2 and $MoSe_2$ light-emitting quantum wells decreased on going from cryogenic conditions to room temperature.[102] On the contrary, the EQE of WSe_2 light-emitting quantum wells increased with temperature. The EQE of the WSe_2 light-emitting quantum wells reached 5%, which was much larger than the EQE of MoS_2 and $MoSe_2$ light-emitting quantum wells in ambient conditions. A performance outline of TMDC LEDs is given in Table 2.

5. Novel LED devices

5.1. Single-photon emitter

Recently, significant progress has been made in realizing efficient single-photon emitters that can be used for quantum information and technology devices. Single-defects in monolayer TMDCs may be a new type of single-photon source.[103–106] Clark *et al.*[24] demonstrated a single-defect emitter by using both vertical and lateral van der Waals heterostructures of monolayer WSe_2. Single-defect emitters are enabled by integration with a variety of optical components such as photonic crystal cavities and waveguides (Fig. 12a).[50] Liu *et al.*[50] demonstrated direct modulation of this single-mode EL at a high speed of ~1 MHz, as seen in Fig. 12b. The high-resolution PL spectrum of the 1L-WSe_2 flake revealed a doublet split by $\Delta = 726$ meV with unequal intensities, as shown in Fig. 12c.[106] A strong antibunched photon emission from this emitter was observed and then confirmed by fit using the relation $g^{(2)}(\tau) = 1 - \rho^2 e^{-|\tau|/T}$ (Fig. 12d).[107] The coupling single photons were detected from discrete quantum emitters in WSe_2, which was also verified *via* the observation of antibunching in the signal ($g^{(2)}(0) = 0.42$).[108] To date, much research has been conducted on single-photon emitters of layered TMDCs utilizing PL; however, little has been done by way of EL. Iff *et al.*[109] showed a compact and hybrid two-dimensional semiconductor-piezoelectric device that allows for controlling the energy of single photons emitted and localized in wrinkled WSe_2 monolayers by strain fields (Fig. 12e).[109] The ensemble emission due to defect-bound excitonic complexes can be seen in both 1L and 2L WSe_2 (Fig. 12f).[107] The realization of electrically driven polariton LEDs in atomically thin semiconductors at room temperature presents a promising step towards achieving an inversionless electrically driven laser, as well as ultrafast microcavity LEDs.[110]

5.2. AC voltage transient EL in TMDCs

Lien *et al.*[64] demonstrated a transient-mode EL device based on TMDC monolayers (including MoS_2, WS_2, $MoSe_2$, and WSe_2). The device structure was MS heterojunction, as shown in Fig. 13a. Pulsed EL was observed at each V_g transition (Fig. 13b). EL from this device was weakly dependent on the Schottky barrier height or polarity. The main factor limiting the performance of the time-EL device is QY droop due to bi-

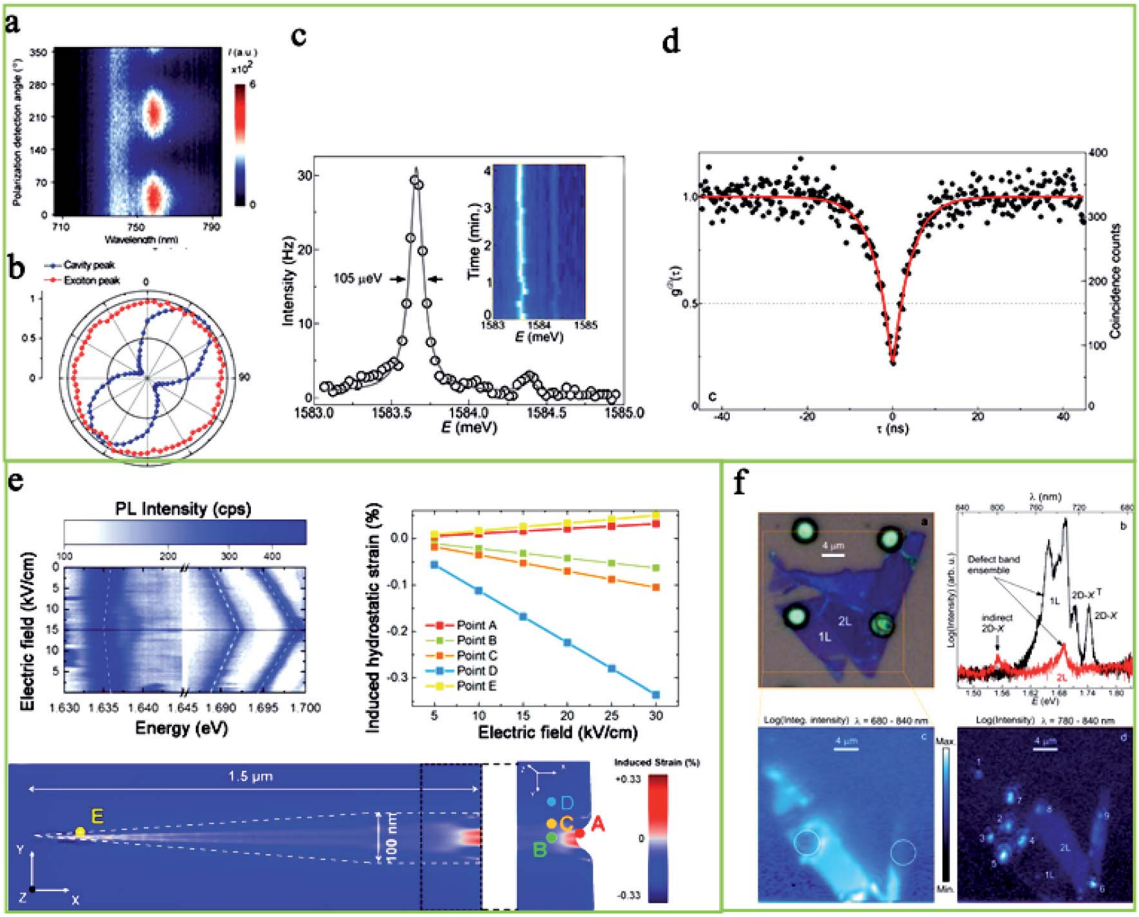

Fig. 12 The performance of a single photon emitter based on layered TMDCs. (a) The measured on-cavity EL as a function of polarization detection angle. (b) Normalized cavity-enhanced peak intensity (blue dots) and exciton peak intensity (red dots) as a function of polarization detection angle. (a and b) Reproduced with permission;[50] Copyright 2017, American Chemical Society. (c) High-resolution PL spectrum of 0D-X from the location of WSe_2 on the p-Si substrate. (d) Normalized second-order correlation function $g^{(2)}(\tau)$ of the 0D-X lines of WSe_2 on the p-Si substrate under non-resonant cw excitation at $P = 0.5P_N$. (e) Contour plot of the PL spectra of SPEs as a function of the electric field applied on a (001) piezoelectric device. Evolution of the hydrostatic strain as a function of the electric field applied to a (001) piezoelectric device calculated on five different points of the wrinkle. Reproduced with permission;[109] Copyright 2019, American Chemical Society. (f) Typical PL emission spectra for 1L (black) and 2L (red) WSe_2 from the smooth and unstrained locations of the flake; color-coded spatial maps of PL with (left) integrated intensities in the spectral range of 680–840 nm, and (right) intensities in the spectral range of 780–840 nm. (c, d and f) Reproduced with permission;[107] Copyright 2015, American Chemical Society.

excitonic recombination. The large voltage drop and the steep energy band bending at the Schottky contact lead to large transient tunneling currents. Injected electrons diffused inward while holes exited the semiconductor through contact or recombination with incoming electrons. In the steady-state, the band bending and tunneling current of the semiconductor and contact decrease. In the alternating current transient process, the excess electron and hole population occur simultaneously. The transient EL was applied to display the letters C–A–L (Fig. 13c). It is rewarding that suspended two-dimensional materials can produce periodic oscillation in the reflection and PL spectra, therefore providing a direct way to fabricate periodic EL devices.[111] Recently, a transient-mode EL device was been fabricated based on WS_2-metal contact; a centimeter-scale ($\approx$0.5 cm^2) visible (640 nm) display was demonstrated, which showcases the potential of TMDC systems for display applications.[112]

5.3. Thermal light emission

Thermoluminescence occurs from a nanomaterial at elevated temperatures, which leads to the thermal propagation of exciton states and the subsequent radiative recombination.[45] High temperatures can be reached by minimizing heat loss in the vertical direction through the substrate or along the lateral direction toward the contact electrodes. The transverse heat flux is determined by the thermal conductivity of the material.[113] Dobusch *et al.*[113] demonstrated that a MoS_2 monolayer sheet, freely suspended in a vacuum over a distance of 150 nm, emitted visible light as a result of Joule heating (Fig. 13d). Due to the poor transfer of heat to the contact electrodes, as well as the suppressed heat dissipation through the underlying substrate, the electron temperature can reach 1500–1600 K, as seen in Fig. 13e and f.[6,113,114] The well-pronounced peak at around 1.7 eV corresponds to the A-exciton of the MoS_2

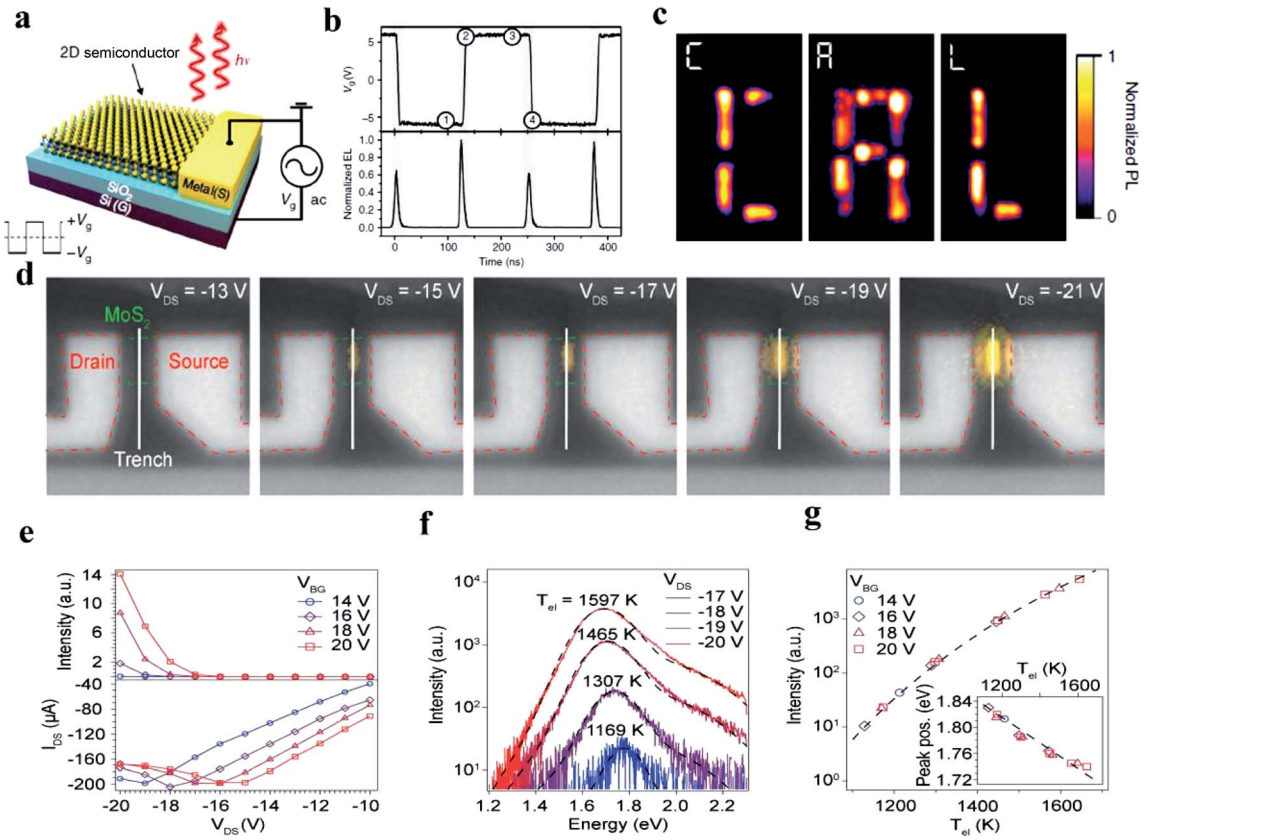

Fig. 13 AC voltage transient EL and thermal light emission from layered TMDCs. (a) Structure diagram of the time-EL device. (b) Time-resolved EL. (c) Operation of the seven-segment display of C–A–L. (a–c) Reproduced with permission.[64] Copyright 2018, Springer Nature. (d) Optical images of the thermal light emitter for various bias conditions, ranging from $V_{DS} = -13$ to -21 V (from left to right). (e) Integrated thermal emission intensity and corresponding current I_{DS} *versus* bias voltage V_{DS} plots. (f) Measured thermal emission spectra. (g) Thermal light emission intensity plotted as a function of temperature. (d–g) Reproduced with permission;[113] Copyright 2017, WILEY-VCH.

monolayer. The second (weaker) peak at higher energy, referring to the B-exciton, arises from the spin–orbit splitting of the valence band and corresponds to the transition from the lower spin level of the valence band (Fig. 13g). Compared to the PL spectra, the thermal emission spectra are usually broader and shifted in energy.

6. Conclusions

Since the EL light intensity and luminescence power of 2D layered TMDCs LEDs is low, it is essential to improve the emission performance of TMDCs LED. It is important to design effective structures to extend the multifunction of TMDC LEDs. Nowadays, the highest EQE of TMDC LEDs is only 12%, which reduces the utilization rate of TMDCs. The low EQE originates from the low quantum yield (QY). It is necessary to take measures to improve the QY of TMDCs. The QY of monolayer MoS_2 was hugely enhanced by organic superacid treatment.[115] This method opens the door for the development of highly efficient LEDs. Hot carriers can be injected into the bandgap of the heterojunction, then electrons may be trapped or form an interfacial state. Therefore, to improve the reliability of electronic devices based on TMDCs, thermal management may be necessary.[113] Otherwise, the control of valley-spin polarization in solids is a basic research area for electronic applications. Further studies on polarization EL are necessary.

The optical band gap of monolayer TMDCs is so narrow that the EL peak wavelength is in the range from infrared light to red light. In order for layered TMDCs heterostructure LEDS to emit visible light in the full spectrum range, they need to be assembled with other wide bandgap materials. Moreover, as a supplement to sunlight, white light is useful in agriculture, for example, in greenhouse plants. It is rare to emit white light from TMDCs LEDs up to ultraviolet light, so TMDC-based white light LEDs may be an important research direction.[116,117] Haldar *et al.*[118] have found white light in MoS_2 QD PL, which provides instructions for the fabrication of white light LEDs in the future. Furthermore, flexible devices are expected to meet the increasing demands for wearable and portable electronics. MoS_2-dependent flexible optoelectronic devices have been fabricated,[119–122] so it may be interesting to prepare flexible LEDs based on TMDCs. MoS_2 with piezo-phototronic effects has been fabricated, which indicates a new direction for the study of other TMDC piezo-phototronic devices.[123] MoS_2 materials have also been used in gas sensors and nanogenerators; this is a potential direction for integrating 2D layered TMDCs LED with other devices such as gas sensors, nanogenerators.[122,124,125]

Conflicts of interest

There are no conflicts of interest to declare.

Acknowledgements

We acknowledge support from the National Natural Science Foundation of China (Grant No. 51705138, 11874025 and 11674113).

Notes and references

1 G. G. D. Han, K. H. Tu, F. Niroui, W. Xu, S. Zhou, X. Wang, V. Bulović, C. A. Ross, J. H. Warner and J. C. Grossman, *Adv. Funct. Mater.*, 2017, **27**, 1703688.
2 N. T. Son, Y.-S. Kim and E. Janzén, *Phys. Status Solidi RRL*, 2015, **9**, 707–710.
3 D. Chiappe, I. Asselberghs, S. Sutar, S. Iacovo, V. Afanas'ev, A. Stesmans, Y. Balaji, L. Peters, M. Heyne, M. Mannarino, W. Vandervorst, S. Sayan, C. Huyghebaert, M. Caymax, M. Heyns, S. De Gendt, I. Radu and A. Thean, *Adv. Mater. Interfaces*, 2016, **3**, 1500635.
4 D. Arcos, D. Gabriel, D. Dumcenco, A. Kis and N. Ferrer-Anglada, *Phys. Status Solidi B*, 2016, **253**, 2499–2504.
5 H. J. Kim, D. Kim, S. Jung, M. H. Bae, Y. J. Yun, S. N. Yi, J. S. Yu, J. H. Kim and D. H. Ha, *J. Raman Spectrosc.*, 2018, **49**, 1938–1944.
6 H. S. Tsai, Y. H. Huang, P. C. Tsai, Y. J. Chen, H. Ahn, S. Y. Lin and Y. J. Lu, *ACS Omega*, 2020, **5**, 10725–10730.
7 R. Caputo, A. Tekin, R. Nesper and Z. Anorg, *Z. Anorg. Allg. Chem.*, 2019, **645**, 309–316.
8 J. B. Cook, H. Kim, T. C. Lin, C. H. Lai, B. Dunn and S. H. Tolbert, *Adv. Energy Mater.*, 2017, **7**, 1601283.
9 G. J. Choi, Q. Van Le, K. S. Choi, K. C. Kwon, H. W. Jang, J. S. Gwag and S. Y. Kim, *Adv. Mater.*, 2017, **29**, 1702598.
10 E. G. da Silveira Firmiano, A. C. Rabelo, C. J. Dalmaschio, A. N. Pinheiro, E. C. Pereira, W. H. Schreiner and E. R. Leite, *Adv. Energy Mater.*, 2014, **4**, 1301380.
11 G. Froehlicher, E. Lorchat and S. Berciaud, *Phys. Rev. B*, 2016, **94**, 085429.
12 H. Coy-Diaz, F. Bertran, C. Chen, J. Avila, J. Rault, P. Le Fèvre, M. C. Asensio and M. Batzill, *Phys. Status Solidi RRL*, 2015, **9**, 701–706.
13 C. Wang, Y. Zhan and Z. Wang, *ChemistrySelect*, 2018, **3**, 1713–1718.
14 J. Shi, R. Tong, X. Zhou, Y. Gong, Z. Zhang, Q. Ji, Y. Zhang, Q. Fang, L. Gu, X. Wang, Z. Liu and Y. Zhang, *Adv. Mater.*, 2016, **28**, 10664–10672.
15 R. Ke, X. Zhang, L. Wang, C. Zhang, S. Zhang, H. Niu, C. Mao, J. Song, B. Jin and Y. Tian, *J. Solid-State Electron Devices*, 2015, **19**, 1633–1636.
16 M. Shrivastava, R. Kumari, M. R. Parra, P. Pandey, H. Siddiqui and F. Z. Hague, *Opt. Mater.*, 2017, **73**, 763–771.
17 W. Su, Y. Wang, W. Wu, H. Qin, K. Song, X. Huang, L. Zhang and D. Chen, *J. Mater. Chem. C*, 2017, **5**, 6352–6358.
18 Y. M. Liu, J. J. Yang, J. T. Cao, J. J. Zhang, Y. H. Chen and S. W. Ren, *Sens. Actuators, B*, 2016, **232**, 538.
19 F. Xu, B. Zhu, B. Cheng, J. Yu and J. Xu, *Adv. Opt. Mater.*, 2018, **6**, 1800911.
20 K. Mallikarjuna, M. A. Shinde and H. Kim, *Mater. Sci. Semicond. Process.*, 2020, **117**, 105176.
21 W. Yin, X. Bai, X. Zhang, J. Zhang, X. Gao and W. W. Yu, *Part. Part. Syst. Charact.*, 2019, **36**, 1800362.
22 A. Capasso, F. Matteocci, L. Najafi, M. Prato, J. Buha, L. Cinà, V. Pellegrini, A. D. Carlo and F. Bonaccorso, *Adv. Energy Mater.*, 2016, **6**, 1600920.
23 Y. Chen, X. Wang, G. Wu, Z. Wang, H. Fang, T. Lin, S. Sun, H. Shen, W. Hu, J. Wang, J. Sun, X. Meng and J. Chu, *Small*, 2018, **14**, 1703293.
24 G. Clark, J. R. Schaibley, J. Ross, T. Taniguchi, K. Watanabe, J. R. Hendrickson, S. Mou, W. Yao and X. Xu, *Nano Lett.*, 2016, **16**, 3944–3948.
25 S. Qiao, R. Cong, J. Liu, B. Liang, G. Fu, W. Yu, K. Ren, S. Wang and C. Pan, *J. Mater. Chem. C*, 2018, **6**, 32–33.
26 X. Zhou, N. Zhou, C. Li, H. Y. Song, Q. Zhang, X. Z. Hu, L. Gan, H. Q. Li, J. T. Lü, J. Luo, J. Xiong and T. Y. Zhai, *2D mater.*, 2017, **4**, 025048.
27 N. Krane, C. Lotze, J. M. Lager, G. Reecht and K. J. Franke, *Nano Lett.*, 2016, **16**, 5163–5168.
28 H. Jeong, R. Salas-Montiel, G. Lerondel and M. S. Jeong, *J. Alloys Compd.*, 2017, **708**, 612–618.
29 Y. Lee and J. Kim, *ACS Photonics*, 2018, **5**, 4187–4194.
30 M. Farkous, M. Bikerouin, H. T. T. Phung, M. El-Yadri, E. Feddi, F. Dujardin, C. A. Duque, D. Muoi, H. V. Phuc, C. V. Nguyen and N. N. Hieu, *Mater. Res. Express*, 2019, **6**, 065060.
31 K. Ren, M. Sun, Y. Luo, S. Wang, Y. Xu, J. Yu and W. Tang, *Phys. Lett. A*, 2019, **383**, 1487–1492.
32 C. B. Qin, Y. Gao, Z. X. Qiao, L. T. Xiao and S. T. Jia, *Adv. Opt. Mater.*, 2016, **4**, 1429–1456.
33 M. Hong, X. B. Zhou, N. Gao, S. L. Jiang, C. Y. Xie, L. Y. Zhao, Y. Gao, Z. P. Zhang, P. F. Yang, Y. P. Shi, Q. Zhang, Z. F. Liu, J. J. Zhao and Y. F. Zhang, *ACS Nano*, 2018, **12**, 10095–10103.
34 Y. Ge, Z. Y. Ding, W. J. Meng, J. H. Wang, Y. B. Hou, G. Wu, Q. Y. Lu and X. P. Yang, *Phys. Rev. B*, 2020, **101**, 104305.
35 F. Bussolotti, J. W. Chai, M. Yang, H. Kawai, Z. Zhang, S. J. Wang, S. L. Wong, C. Manzano, Y. L. Huang, D. Z. Chi and K. E. J. Goh, *RSC Adv.*, 2018, **8**, 7744–7752.
36 F. Zhang, Z. X. Lu, Y. C. Choi, H. N. Liu, H. S. Zheng, L. M. Xie, K. Park and L. Y. Jiao, *ACS Appl. Nano Mater.*, 2018, **1**, 2041–2048.
37 J. He, J. Su, Z. Lin, S. Zhang, Y. Qin, J. Zhang, J. Chang and Y. Hao, *J. Phys. Chem. C*, 2019, **123**, 7158–7165.
38 X. Liu, Z. Li and J. Phys, *Chem. Lett.*, 2015, **6**, 3269–3275.
39 X. Hu, Q. Zhang and S. Yu, *Appl. Surf. Sci.*, 2019, **478**, 857–865.
40 A. Rahman, H. J. Kim, M. Noor-A-Alam and Y.-H. Shin, *Curr. Appl. Phys.*, 2019, **19**, 709–714.
41 A. T. Hanbicki, H. J. Chuang, M. R. Rosenberger, C. S. Hellberg, S. V. Sivaram, K. M. McCreary, I. I. Mazin and B. T. Jonker, *ACS Nano*, 2018, **12**, 4719–4726.
42 F. Zhang, W. Li and X. Q. Dai, *Solid State Commun.*, 2017, **266**, 11–15.

43 Y. Li, N. Stolte, B. K. Li, H. Li, G. H. Cheng, D. Pan and J. N. Wang, *Nanoscale*, 2019, **11**, 13552–13557.
44 S. Y. Chen, T. Goldstein, T. Taniguchi, K. Watanabe and J. Yan, *Nat. Commun.*, 2018, **9**, 3717.
45 J. Wang, I. Verzhbitskiy and G. Eda, *Adv. Mater.*, 2018, **30**, 1802687.
46 K. Zhang, M. Peng, W. Wu, J. Guo, G. Gao, Y. Liu, J. Kou, R. Wen, Y. Lei, A. Yu, Y. Zhang, J. Zhai and Z. L. Wang, *Mater. Horiz.*, 2017, **4**, 274–280.
47 A. Ghorai, S. Bayan, N. Gogurla, A. Midya and S. K. Ray, *ACS Appl. Mater. Interfaces*, 2017, **9**, 558–565.
48 C. Palacios-Berraquero, M. Barbone, D. M. Kara, X. Chen, I. Goykhman, D. Yoon, A. K. Ott, J. Beitner, K. Watanabe, T. Taniguchi, A. C. Ferrari and M. Atature, *Nat. Commun.*, 2016, **7**, 12978.
49 Y. W. Sheng, T. X. Chen, Y. Lu, R. J. Chang, S. Sinha and J. H. Warner, *ACS Nano*, 2019, **4**, 4530–4537.
50 C. H. Liu, G. Clark, T. Fryett, S. f. Wu, J. J. Zheng, F. Hatami, X. D. Xu and A. Majumdar, *Nano Lett.*, 2017, **17**, 200–205.
51 Y. Q. Bie, G. Grosso, M. Heuck, M. M. Furchi, Y. Cao, J. Zheng, D. Bunandar, E. Navarro-Moratalla, L. Zhou, D. K. Efetov, T. Taniguchi, K. Watanabe, J. Kong, D. Englund and P. Jarillo-Herrero, *Nat. Nanotechnol.*, 2017, **12**, 1124–1129.
52 F. Xue, L. Yang, M. Chen, J. Chen, X. Yang, L. Wang, L. Chen, C. Pan and Z. L. Wang, *NPG Asia Mater.*, 2017, **9**, e418.
53 R. Cheng, D. Li, H. Zhou, C. Wang, A. Yin, S. Jiang, Y. Liu, Y. Chen, Y. Huang and X. Duan, *Nano Lett.*, 2014, **14**, 5590–5597.
54 M. Y. Li, J. Pu, J. K. Huang, Y. H. Miyauchi and K. Matsuda, *Adv. Funct. Mater.*, 2018, **28**, 1706860.
55 Y. Jin, D. H. Keum, S. J. An, J. Kim, H. S. Lee and Y. H. Lee, *Adv. Mater.*, 2015, **27**, 5534–5540.
56 H. M. Li, D. Lee, D. Qu, X. Liu, J. Ryu, A. Seabaugh and W. J. Yoo, *Nat. Commun.*, 2015, **6**, 6564.
57 O. L. Sanchez, E. A. Llado, V. Koman, A. F. Morral, A. Radenovic and A. Kis, *ACS Nano*, 2014, **8**, 3042–3048.
58 K. Nishiguchi, A. Castellanos-Gomez, H. Yamaguchi, A. Fujiwara, H. S. J. van der Zant and G. A. Steele, *Appl. Phys. Lett.*, 2015, **107**, 053101.
59 S. Jo, N. Ubrig, H. Berger, A. B. Kuzmenko and A. F. Morpurgo, *Nano Lett.*, 2014, **14**, 2019–2025.
60 Y. Zhang, R. Suzuki and Y. Iwasa, *ACS Nano*, 2017, **11**, 12583–12590.
61 B. W. Baugher, H. O. Churchill, Y. Yang and P. Jarillo-Herrero, *Nat. Nanotechnol.*, 2014, **9**, 262–267.
62 A. A. El Yumin, J. Yang, Q. Chen, O. Zheliuk and J. Ye, *Phys. Status Solidi B*, 2017, **254**, 1700180.
63 S. Mukherjee, R. Maiti, A. K. Katiyar, S. Das and S. K. Ray, *Sci. Rep.*, 2016, **6**, 29016.
64 D. H. Lien, M. Amani, S. B. Desai, G. H. Ahn, K. Han, J. H. He, J. W. Ager III, M. C. Wu and A. Javey, *Nat. Commun.*, 2018, **9**, 1229.
65 R. P. Puchert, F. Steiner, G. Plechinger, F. J. Hofmann, I. Caspers, J. Kirschner, P. Nagler, A. Chernikov, C. Schuelle, T. Korn, J. Vogelsang, S. Bange and J. M. Lupton, *Nat. Nanotechnol.*, 2017, **12**, 637–641.
66 X. Zhang, W. Guo, Z. Wang, H. Ke, W. Zhao, A. Zhang, C. Huang and N. Jia, *Sens. Actuators, B*, 2017, **253**, 470–477.
67 K. J. Reynolds, J. A. Barker, N. C. Greenham, R. H. Friend and G. L. Frey, *J. Appl. Phys.*, 2002, **92**, 7556–7563.
68 X. W. Zhang, W. S. Li, Z. T. Ling, Y. Zhang, J. W. Xu, H. Wang, G. H. Chen and B. Wei, *J. Mater. Chem. C*, 2019, **7**, 926–936.
69 J. S. Ross, P. Klement, A. M. Jones, N. J. Ghimire, J. Yan, D. G. Mandrus, T. Taniguchi, K. Watanabe, K. Kitamura, W. Yao, D. H. Cobden and X. Xu, *Nat. Nanotechnol.*, 2014, **9**, 268–272.
70 G. Gupta and K. Majumdar, *Phys. Rev. B*, 2019, **99**, 085412.
71 I. Gutierrez-Lezama, B. A. Reddy, N. Ubrig and A. F. Morpurgo, *2D Mater.*, 2016, **3**, 045016.
72 Y. Rong, Y. Sheng, M. Pacios, X. Wang, Z. He, H. Bhaskaran and J. H. Warner, *ACS Nano*, 2016, **10**, 1093–1110.
73 Y. Ye, Z. Ye, M. Gharghi, X. Yin, H. Zhu, M. Zhao and X. Zhang, *Appl. Phys. Lett.*, 2014, **104**, 193508.
74 R. S. Sundaram, M. Engel, A. Lombardo, R. Krupke, A. C. Ferrari, P. Avouris and M. Steiner, *Nano Lett.*, 2013, **13**, 1416–1421.
75 W. Yang, J. Shang, J. Wang, X. Shen, B. Cao, N. Peimyoo, C. Zou, Y. Chen, Y. Wang, C. Cong, W. Huang and T. Yu, *Nano Lett.*, 2016, **16**, 1560–1567.
76 Y. Li, J. Shi, H. Chen, R. Wang, Y. Mi, C. Zhang, W. Du, S. Zhang, Z. Liu, Q. Zhang, X. Qiu, H. Xu, W. Liu, Y. Liu and X. Liu, *Nanoscale*, 2018, **10**, 17585–17592.
77 S. Schwarz, A. Kozikov, F. Withers, J. K. Maguire, A. P. Foster, S. Dufferwie, L. Hague, M. N. Makhonin, L. R. Wilson, A. K. Geim, K. S. Novoselov and A. I. Tartakovskii, *2D Mater.*, 2016, **3**, 025038.
78 A. Pospischil, M. M. Furchi and T. Mueller, *Nat. Nanotechnol.*, 2014, **9**, 257–261.
79 M. Paur, A. J. Molina-mendoza and T. Mueller, *Nat. Commun.*, 2019, **10**, 1709.
80 Z. L. Wen, C. J. Zhang, Z. M. Zhou, B. Xu, K. Wang, K. L. Teo and X. W. Sun, *IEEE J. Quantum Electron.*, 2020, **56**, 3200106.
81 P. Perumal, C. Karuppiah, W. C. Liao, Y. R. Liou, Y. M. Liao and Y. F. Chen, *Sci. Rep.*, 2017, **7**, 10002.
82 Z. Chen, H. Liu, X. Chen, G. Chu, S. Chu and H. Zhang, *ACS Appl. Mater. Interfaces*, 2016, **8**, 20267–20273.
83 R. D. Nikam, P. A. Sonawane, R. Sankar and Y. T. Chen, *Nano Energy*, 2017, **32**, 454–462.
84 D. Andrzejewski, H. Myja, M. Heuken, A. Grundmann, H. Kalisch, A. Vescan, T. Kummell and G. Bacher, *ACS Photonics*, 2019, **6**, 1832–1839.
85 E. Ponomarev, I. Gutierrez-Lezama, N. Ubrig and A. F. Morpurgo, *Nano Lett.*, 2015, **15**, 8289–8294.
86 D. Li, R. Cheng, H. Zhou, C. Wang, A. Yin, Y. Chen, N. O. Weiss, Y. Huang and X. Duan, *Nat. Commun.*, 2015, **6**, 7509.
87 Y. Zhu, Z. Li, L. Zhang, B. Wang, Z. Luo, J. Long, J. Yang, L. Fu and Y. Lu, *ACS Appl. Mater. Interfaces*, 2018, **50**, 43291–43298.

88 P. Li, K. Yuan, D. Y. Lin, X. l. Xu, Y. l. Wang, Y. Wan, H. R. Yu, K. Zhang, Y. Ye and L. Dai, *Nanoscale*, 2017, **9**, 18175–18179.
89 S. Y. Zheng, J. K. So, K. Liu, F. C. Liu, L. Zheng, N. Zheludev and H. J. Fan, *Nano Lett.*, 2017, **17**, 6475–6480.
90 J. Schaibley, M. Betz and A. Y. Elezzabi, *In conference of Ultrafast Phenomena and Nanophotonics Xxi*, Hamburg, Germany, 23 February, 2017.
91 J. Y. Wang, F. Lin, I. Verzhbitskiy, K. J. Watanabe, T. Taniguchi, J. Martin and G. Eda, *Nano Lett.*, 2019, **19**, 7470–7475.
92 Y. J. Zhang, T. Oka, R. Suzuki, J. T. Ye and Y. Iwasa, *Science*, 2014, **344**, 725–728.
93 Y. Ye, J. Xiao, H. L. Wang, Z. L. Ye, H. Y. Zhu, M. Zhao, Y. Wang, J. H. Zhao, X. B. Yin and X. Zhang, *Nat. Nanotechnol.*, 2016, **11**, 11598–11602.
94 Y. Z. Li, H. Sun, L. Gan, J. X. Zhang, J. B. Feng, D. Y. G. Zhang and C. Z. Ning, *Proc. IEEE*, 2020, **108**, 676–703.
95 S. Kapatel, C. K. Sumesh, P. Pataniya, G. K. Solanki and K. D. Patel, *Eur. Phys. J. Plus*, 2017, **132**, 191.
96 S. M. Sze and K. K. Ng, *Physics of Semiconductor Devices*, Wiley, Hoboken, NJ, USA, 2007.
97 M. El-Tahchi, A. Khoury, M. De Labardonnie, P. Mialhe and F. Pelanchon, *Sol. Energy Mater. Sol. Cells*, 2000, **62**, 393–398.
98 T. H. Peng, C. H. Hong, M. R. Tang and S. C. Leeb, *AIP Adv.*, 2019, **9**, 075010.
99 X. Huang, X. W. Feng, L. Chen, L. Wang, W. C. Tan, L. Huang and K. W. Ang, *Nano Energy*, 2019, **62**, 667–673.
100 H. V. Han, A. Y. Lu, L. S. Lu, J. K. Huang, H. Li, C. L. Hsu, Y. C. Lin, M. H. Chiu, K. Suenaga, C. W. Chu, H. C. Kuo, W. H. Chang, L. J. Li and Y. Shi, *ACS Nano*, 2016, **10**, 1454–1461.
101 S. K. Han, X. Y. Yang, Y. H. Zhu, C. L. Tan, X. Zhang, J. Z. Chen, Y. Huang, B. Chen, Z. M. Luo, Q. L. Ma, M. Sindoro, H. Zhang, X. Y. Qi, H. Li, X. Huang, W. Huang, X. W. Sun, Y. Han and H. Zhang, *Angew. Chem., Int. Ed.*, 2017, **56**, 10486–10490.
102 F. Withers, O. Del Pozo-Zamudio, S. Schwarz, S. Dufferwiel, P. M. Walker, T. Godde, A. P. Rooney, A. Gholinia, C. R. Woods, P. Blake, S. J. Haigh, K. Watanabe, T. Taniguchi, I. L. Aleiner, A. K. Geim, V. I. Fal'ko, A. I. Tartakovskii and K. S. Novoselov, *Nano Lett.*, 2015, **15**, 8223–8228.
103 A. Srivastava, M. Sidler, A. V. Allain, D. S. Lembke, A. Kis and A. Imamoğlu, *Nat. Phys.*, 2015, **11**, 141–147.
104 C. Chakraborty, L. Kinnischtzke, K. M. Goodfellow, R. Beams and A. N. Vamivakas, *Nat. Nanotechnol.*, 2015, **10**, 507–511.
105 M. Koperski, K. Nogajewski, A. Arora, V. Cherkez, P. Mallet, J. Y. Veuillen, J. Marcus, P. Kossacki and M. Potemski, *Nat. Nanotechnol.*, 2015, **10**, 503–506.
106 P. Tonndorf, R. Schmidt, R. Schneider, J. Kern, M. Buscema, G. A. Steele, A. Castellanos-Gomez, H. S. J. van der Zant, S. Michaelis de Vasconcellos and R. Bratschitsch, *Optica*, 2015, **2**, 347–352.
107 S. Kumar, A. Kaczmarczyk and B. D. Gerardot, *Nano Lett.*, 2015, **15**, 7567–7573.
108 M. Blauth, M. Jürgensen, G. Vest, O. Hartwig, M. Prechtl, J. Cerne, J. J. Finley and M. Kaniber, *Nano Lett.*, 2018, **18**, 6812–6819.
109 O. Iff, D. Tedeschi, J. Martín-Sánchez, M. Moczała-Dusanowska, S. Tongay, K. Yumigeta, J. Taboada-Gutiérrez, M. Savaresi, A. Rastelli, P. Alonso-González, S. Höfling, R. Trotta and C. Schneider, *Nano Lett.*, 2019, **19**, 6931–6936.
110 J. Gu, B. Chakraborty, M. Khatoniar and V. M. Menon, *Nat. Nanotechnol.*, 2019, **14**, 1024–1028.
111 M. Yoshita, H. Kubota, M. Shimogawara, K. Mori, Y. Ohmiya and H. Akiyama, *Rev. Sci. Instrum.*, 2017, **88**, 093704.
112 J. Cho, M. Amani, D. H. Lien, H. Kim, M. Yeh, V. Wang, C. L. Tan and A. Javey, *Adv. Funct. Mater.*, 2020, **30**, 1907941.
113 L. Dobusch, S. Schuler, V. Perebeinos and T. Mueller, *Adv. Mater.*, 2017, **29**, 1701304.
114 G. Deokar, P. Vancsó, R. Arenal, F. Ravaux, J. C. Cháfer, E. Llobet, A. Makarova, D. Vyalikh, C. Struzzi, P. Lambin, M. Jouiad and J. F. Colomer, *Adv. Mater. Interfaces*, 2017, **4**, 1700801.
115 M. Amani, D. H. Lien, D. Kiriya, J. Xiao, A. Azcatl, J. Noh, S. R. Madhvapathy, R. Addou, S. Kc, M. Dubey, K. Cho, R. M. Wallace, S. C. Lee, J. H. He, J. W. Ager, X. Zhang, E. Yablonovitch and A. Javey, *Science*, 2015, **350**, 1065–1068.
116 G. Z. Lu, M. J. Wu, T. N. Lin, C. Y. Chang, W. L. Lin, Y. T. Chen, C. F. Hou, H. J. Cheng, T. Y. Lin, J. L. Shen and Y. F. Chen, *Small*, 2019, **15**, 1901908.
117 W. X. Yin, X. Bai, P. Chen, X. Y. Zhang, L. Su, C. Y. Ji, H. M. Gao, H. W. Song and W. W. Yu, *ACS Appl. Mater. Interfaces*, 2018, **10**, 43824–43830.
118 M. H. He, Y. J. Lin, C. M. Chiu, W. F. Yang, B. B. Zhang, D. Q. Yun, Y. N. Xie, Z. H. Lin, D. Haldar, A. Ghosh, S. Bose, S. Mondal, U. K. Ghorai and S. K. Saha, *Opt. Mater.*, 2018, **79**, 12–20.
119 F. Yu, M. Hu, F. Kang and R. Lv, *Prog. Nat. Sci.: Mater. Int.*, 2018, **28**, 563–568.
120 S. Bhattacharjeea, U. Dasa, P. K. Sarkarb and A. Roya, *Org. Electron.*, 2018, **58**, 145–152.
121 B. Sun, T. Shi, Z. Y. Liu, Y. Wu, J. X. Zhou and G. L. Liao, *Mater. Des.*, 2018, **154**, 1–7.
122 M. H. He, Y. h. Lin, C. M. Chiu, W. F. Yang, B. B. Zhang, D. Q. Yun, Y. N. Xie and Z. H. Lin, *Nano Energy*, 2018, **49**, 588–595.
123 K. Zhang, J. Y. Zhai and Z. L. Wang, *2D Mater.*, 2018, **5**, 035038.
124 M. W. Jung, S. M. Kang, K. H. Nam, K. S. An and B. C. Ku, *Appl. Surf. Sci.*, 2018, **456**, 7–12.
125 X. Ou, C. Fang, Y. Fan, H. Chen, S. Chen and S. Wei, *Sens. Actuators, B*, 2016, **228**, 625–633.

